Comparative Evaluation of LMR-NCM and NCA Cathode Active Materials in Multilayer Lithium-Ion Pouch Cells: Part I. Production, Electrode Characterization, and Formation

David Schreiner,[1,=,z] Tanja Zünd,[2,=,*] Florian J. Günter,[1] Ludwig Kraft,[3,*] Benedikt Stumper,[1] Fabian Linsenmann,[2] Michael Schüßler,[1] Rebecca Wilhelm,[2,*] Andreas Jossen,[3] Gunther Reinhart,[1] and Hubert A. Gasteiger[2,**]

[1]*Institute for Machine Tools and Industrial Management, Technical University of Munich, D-85748 Garching, Germany*
[2]*Chair of Technical Electrochemistry, Technical University of Munich, D-85748 Garching, Germany*
[3]*Institute for Electrical Energy Storage Technology, Technical University of Munich, D-80333 Munich, Germany*

A lithium- and manganese-rich layered transition metal oxide (LMR-NCM) cathode active material (CAM) is processed on a pilot production line and assembled with graphite anodes to ≈7 Ah multilayer pouch cells. Each production step is outlined in detail and compared to NCA/graphite reference cells. Using laboratory coin cell data for different CAM loadings and cathode porosities, a simple calculation tool to extrapolate and optimize the energy density of multilayer pouch cells is presented and validated. Scanning electron microscopy and mercury porosimetry measurements of the cathodes elucidate the effect of the CAM morphology on the calendering process and explain the difficulty of achieving commonly used cathode porosities with LMR-NCM cathodes. Since LMR-NCMs exhibit strong gassing during the first cycles, a modified formation procedure based on on-line electrochemical mass spectroscopy is developed that allows stable cycling of LMR-NCM in multilayer pouch cells. After formation and degassing, LMR-NCM/graphite pouch cells have a 30% higher CAM-specific capacity and a ≈5%–10% higher cell-level energy density at a rate of C/10 compared to NCA/graphite cells. Rate capability, long-term cycling, and thermal behavior of the pouch cells in comparison with laboratory coin cells are investigated in Part II of this work.

Since the commercialization of lithium-ion batteries (LIBs), the cathode active material (CAM) capacity has been the limitation for increasing the energy density of LIB cells and battery packs.[1–3] In addition to the performance and safety,[4,5] cathode active materials have a significant impact on the price of LIBs because of the high raw material costs for nickel and cobalt containing CAMs.[6,7] Lithium- and manganese-rich nickel-cobalt-manganese oxides (LMR-NCM) offer high reversible specific capacities up to 280 mAh g^{-1} [8–10] and show a significant cost advantage over Ni-rich NCMs due to the roughly one order of magnitude lower raw material cost of manganese (2 USD kg^{-1})[11] compared to nickel (21 USD kg^{-1}).[11,12] In contrast to these advantages, there are still challenges to overcome for the commercialization of LMR-NCM, such as the observed discharge voltage fading,[10,13–15] the oxygen release in the first few cycles[16] from the near-surface region of the material,[10,17] and a pronounced charge-discharge voltage hysteresis.[1,18]

LMR-NCM cells with high reversible capacities over several hundred cycles have already been demonstrated on a laboratory scale (typically using coin cells) for optimized material compositions, surface coatings, and tailored electrolytes.[9,10,19] Thus, many promising results have been reported for LMR-NCM CAMs at the coin cell level, which, however, are usually based on small CAM loadings (e.g., 3–7 mg$_{CAM}$/cm^2)[19–22] that are typically assembled with 50–120 μl of electrolyte, resulting in a high mass ratio of electrolyte to CAM (e.g., $mass_{electrolyte}/mass_{CAM}$ of 13/1 to 48/1).[20,21] Only very few examples can be found in the literature, where full-cell coin cells were assembled with such low amounts of electrolyte that result in $mass_{electrolyte}/mass_{CAM}$ ratios (e.g., $mass_{electrolyte}/mass_{CAM}$ of ≈ 1.6/1[10,23]) that more closely approach those in large-scale cells, viz., $mass_{electrolyte}/mass_{CAM} ≈ 1/1$,[24] also used for the multilayer pouch cells produced in this work (see *Production step 10: electrolyte filling* in the Experimental section). Since

the amount of electrolyte in the cell, often expressed in terms of the $mass_{electrolyte}/mass_{CAM}$ ratio (sometimes also as $mass_{electrolyte}/Ah$)[25,26] is known to critically affect the cycle-life when using active materials with intrinsically low coulombic efficiency (e.g., with silicon based[27,28] or with lithium metal anodes[26]) and/or when using electrolyte additives,[29,30] a rigorous evaluation of new active materials, particularly with regards to cycle-life, can only be obtained by tests with large-scale cells (e.g., with the here used multilayered, large-format pouch cells).

Since the costs for battery cells mainly depend on the costs of the cathode active material[6,7] and the scrap rates within the production,[6,7,31] special attention should be paid to minimize the CAM raw materials costs and to precise process control.[6] Throughout the entire process chain, flaws and uncertainties in the production process are propagated accumulated, which significantly decreases the overall yield.[6] SCHMIDT et al.[32] described and analyzed this propagation of production uncertainties along the process chain and illustrate their influence on the final battery cell.

This paper provides a guideline for each production step of LMR-NCM/graphite cells in comparison to NCA/graphite cells, and also highlights the additional challenges of fabricating LMR-NCM/graphite large-scale multilayer pouch cells compared to small-scale laboratory coin cells. The ability to produce both types of cells, starting from the formulation and mixing of electrode coating slurries all the way to the formation of the finally obtained battery cells using manual methods as well as the pilot scale production line at the Technical University of Munich[33] makes it possible to compare the effects of each production step on the final performance of the cells and to determine the accuracy with which the gravimetric and volumetric energy density of large-scale cells can be projected based on coin cell data. Furthermore, additional ex-situ and operando characterization tools were used to study the influence of the individual process parameters in the various steps to produce laboratory coin cells and multilayer pouch cells, which yielded new insights with regards to the relationship between active material properties, their processability, and the final cell performance.

The here investigated process steps start with the mixing procedure of the individual electrode materials, followed by the coating process. The electrodes are then calendered to the targeted

=These authors contributed equally to this work.
*Electrochemical Society Student Member.
**Electrochemical Society Fellow.
zE-mail: david.schreiner@tum.de

thickness to achieve the desired electrode density or porosity, a step that is required to increase the energy density of the final cells as well as to improve the electrical conductivity across the electrode[34] and to minimize the contact resistance between the cathode electrode coating and the current collector.[35] Depending on the desired application and composition of the electrodes, they are generally calendered from an initial porosity of 45%–60% to typically 18%–35%.[1,6,36,37] Depending on the chosen active materials, the lower limit for the electrode porosity can be posed by either limitation in electrode wetting[38] or the onset of mechanical breakage of the active material particles.[39,40] Since the cell performance and rate capability significantly depend on the ionic and electrical conductivity across the electrode thickness,[34] which in turn depend on the extent of electrode compaction and electrode porosity, it is necessary to carefully investigate the calendering-induced changes of the electrode pore size distribution, which can be done using mercury porosimetry.[41] The achievable compaction of electrodes depends strongly on the morphology of the chosen CAM and can only partially be compensated by using heated calendering rolls,[42–44] or the close adequate conductive carbon black components.[45]

The other investigated production steps, which differ significantly between preparing large-format cells and laboratory-type coin cells, are the processes of filling the cells with electrolyte and cell formation. A large number of influencing factors in the electrolyte filling process[46] and the relationships between the electrolyte filling process, the wetting of the porous materials in the cell with electrolyte, as well as the cell formation and degassing procedure for a given cell format[47] result in a great variety in the currently used process designs that are described in the literature.[48] Degassing is necessary for large-format cells during their initial formation, since with an increased amount of active material, the gas produced during the first charge increases proportionally with the amount of active material or with the number of electrode layers, while the cell volume stays almost the same in stacked cells that are sealed under vacuum. Therefore, the degassing process is an important part of the large-format cell process chain (in contrast to small-scale cells), and removing the gas produced during or after the first charge and discharge cycle is an industrial standard,[49] even though it is scarcely considered in the literature.

Since studies of small-scale laboratory cells can therefore not fully address all the aspects that need to be considered for the manufacturing of large-format cells, this work examines the production steps of multilayered pouch cells with a target capacity of 5.5 Ah at a discharge rate of 1C (corresponding to ≈6–7 Ah at C/10). For this purpose, full-cells with two different cathode active materials are considered, either lithium- and manganese-rich NCM (LMR-NCM) or NCA, highlighting the various challenges in the large-format cell production process and examining the particular differences between the preparation of small-scale cells and large-format cells. A focus of this paper is the often neglected process step of electrode calendering in the preparation of small-scale cells, for which the electrodes are frequently only compressed[20,21,50] by applying a constant compression force rather than being calendered or are even non-compacted at all.[14,19,22]

It will be shown that it is not possible to compact LMR-NCM electrodes to commonly used cathode porosities (≈30%–35%) with the same process parameters used for NCA. The differences in pore size distribution and electrode structure for the two CAMs will be examined by mercury porosimetry and scanning electron microscopy (SEM) cross-sectional analysis. Finally, material adapted calendering parameters are given that allow further processing. Mercury porosimetry is introduced as a method to allow CAM developers to predict the later compaction potential of synthesized CAMs without the possibility of testing it on an industrial calendar. The formation/degassing procedures used for conventional CAMs (e.g., NCM and NCA) cannot be used for LMR-NCM based cells due to the strong first-cycle gassing of this material. Therefore an optimized procedure for the formation and degassing of large-format LMR-NCM/graphite cells is developed using on-line electrochemical mass spectrometry (OEMS) measurements.[51] We also compare the cell performance after the formation of the two cell chemistries on both the material and the cell level, and compare the results with the up-scale prediction based on coin cell pre-experiments. The rate capability, long-term stability, and thermal behavior of the produced large-format multilayer pouch cells are described in Part II of this study.[52]

Experimental

Production of multilayer pouch cells.—The multilayer pouch cells were produced on the pilot scale production line[33] at the Institute for Machine Tools and Industrial Management (*iwb*) of the Technical University of Munich (TUM). The electrode production with the process steps mixing, coating, drying, and calendering took place in a clean room class 1000/ISO 6. The following process steps of the cell assembly were carried out on a semi-automated assembly line in a dry room with a dew point of −40 °C. To support the discussion of each process step and the corresponding process parameters, Fig. 1 provides an overview of the entire process chain of the multilayer pouch cell production at the *iwb* (processes conducted in the clean are gray colored, those in the dry room are blue colored). Additional cell setup information can be found in the attached Excel-based *cell configuration tool* in the supporting information (available online at stacks.iop.org/JES/168/030507/mmedia), where all masses and

Figure 1. Schematic of the battery production process chain of lithium-ion pouch cells at the *iwb*, divided into electrode production (upper row) and cell assembly (lower row). The electrode production consists of the process steps mixing (1), coating and drying (2), calendering (3) conducted in a clean room (gray colored), as well as vacuum drying of the coils conducted in the dry room with a dew point of −40 °C (blue colored). The cell assembly includes confectioning (5), electrode stacking (6), contacting of the electrode stack (7), packaging (8), vacuum drying of the open pouch cells (9), electrolyte filling (10), as well as the formation and degassing of the cells (11), all of which is conducted in a dry room (blue colored) with a dew point of −40 °C.

geometrical information for the multilayer pouch cells prepared here are listed.

Production step 1: mixing.—The slurry for cathode electrode preparation consists of 92.5 wt% cathode active material, i.e., either LMR-NCM (Li$_{1.14}$[Ni$_{0.26}$Co$_{0.14}$Mn$_{0.60}$]$_{0.86}$O$_2$, which can as well be written as 0.33 Li$_2$MnO$_3$ · 0.67 LiNi$_{0.38}$Co$_{0.21}$Mn$_{0.41}$O$_2$ done by Teufl et al.,[10] BASF, Germany) or NCA (LiNi$_{0.81}$Co$_{0.15}$Al$_{0.04}$O$_2$, BASF, Germany) with bulk densities (ρ_{CAM}) of 4.35 g cm^{-3} and 4.65 g cm^{-3}, respectively, 4 wt% conductive carbon black (Super-C65, Timcal, Switzerland, with a bulk density of ρ_{CB} = 2.0 g cm^{-3}), and 3.5 wt% polyvinylidene-fluoride binder (PVdF, Solef 5130, Solvay, Belgium, with a bulk density of ρ_{PVdF} = 1.76 g cm^{-3}). In the context of this work, an electrode is defined as the electrode layer composed of active material, binder, and conductive carbon blacks coated onto the current collector foil), i.e., a cathode consists of an aluminum foil, cathode active material, binder, and conductive carbon blacks. The mixing process was carried out with a Speedmixer DAC 3000.1 HP (Hauschild & Co, Germany), whereby the detailed mixing parameters are listed in the Appendix (Fig. A·1). First, the cathode active materials (CAMs) were dry mixed; subsequently, the solids content was reduced sequentially by adding aliquots of anhydrous N-methyl-2-pyrrolidone (NMP) (Sigma-Aldrich, USA). For LMR-NCM based cathodes, the final solids content was set to 58 wt% (Fig. A·1), whereas for NCA a solids content of 70 wt% was used. The lower solids content for LMR-NCM slurries was required due to its a larger Brunauer-Emmet-Teller (BET) specific surface area and its smaller secondary agglomerate diameter determined by laser scattering (BET = 4.35 m^2 g^{-1}, d$_{50}$ = 10 ± 1 μm diameter) compared to NCA (BET = 0.26 m^2 g^{-1}, d$_{50}$ = 15 ± 1 μm). The rheological properties of the slurries were determined with the MCR 302 rheometer (Anton Paar, Austria) using a plate-plate configuration (with a diameter of 25 mm and a gap of 250 μm) and a test procedure that measured the viscosity vs. the shear rate. At a shear rate of 100 1/s, the viscosity of the LMR-NCM slurry was 3.5 Pa·s and that of the NCA slurry was 10.9 Pa·s. The recommended cathode viscosity in the literature is 5 Pa·s at a shear rate of 100 1/s.[53] Based on our experience, cathode slurries with viscosities between ≈3–12 Pa·s at 100 1/s are coatable with the doctor blade.

The slurry for anode preparation (for mixing parameters see Appendix, Fig. A·1) consists of 97 wt% graphite (SGL Carbon SE, Germany, with a bulk density of ρ_G = 2.26 g cm^{-3}), 1.5 wt% styrene-butadiene rubber (SBR, Zeon Europe GmbH, Japan, with a bulk density of ρ_{SBR} = 1.04 g cm^{-3}), and 1.5 wt% carboxymethyl cellulose (CMC Sunrose MAC200, NPI, Japan, with a bulk density of ρ_{CMC} = 1.6 g cm^{-3}). Deionized water was premixed with CMC (4.43 wt% solids content), then graphite was added to that solution (to an initial solids content of 75 wt%) and further mixed by sequentially adding deionized water to obtain a final solids content of 57 wt%. Finally, the SBR water mixture (40 wt% solids content) was added and mixed for 5 min at 400 rpm. At a shear rate of 100 1/s, the viscosity of the final anode slurry was ≈6–7 Pa·s.

Production step 2: coating and drying.—The cathodes were coated onto both sides of the aluminum current collector foil (15 μm; type 1050 A from Korff, Switzerland) at a speed of 1 m min^{-1}. For the LMR-NCM cathode active material, the average CAM loading per side is 11.7 ± 0.2 mg cm^{-2} (corresponding to ≈2.9 mAh cm^{-2} based on a nominal specific capacity of 250 mAh g^{-1}), resulting in an uncalendered dry electrode thickness of ≈160 μm (this corresponds to the thickness of two cathode coatings and one aluminum current collector); the average weight fraction of the aluminum (wt%$_{alu}$) of the double-sided LMR-NCM electrodes is 13.8%. The constant temperatures for the three dryers were set to 85 °C, 105 °C, and 125 °C. The graphite anodes for the LMR-NCM/graphite cells were coated at a speed of 0.5 m min^{-1} onto both sides of a 11 μm thick copper current collector foil (Cu-PHC, hard rolled blank, with

a nominal thickness of 12 μm, Schlenk, Germany). The average anode active material (AAM) loading per side is 9.5 ± 0.6 mg cm^{-2} (corresponding to ≈3.4 mAh cm^{-2} based on a nominal specific capacity of 355 mAh g^{-1}), resulting in an uncalendered electrode thickness of ≈208 μm (corresponding to the thickness of two anode coatings and one copper current collector) after drying (a temperature of 50 °C was set for all three infrared dryers).

The NCA slurry was also coated double-sided at 1 m min^{-1} onto the same 15 μm thick aluminum foil. The average CAM loading per side is 13.0 ± 0.4 mg cm^{-2} (corresponding to ≈2.6 mAh cm^{-2} based on a nominal specific capacity of 200 mAh g^{-1}), resulting in an uncalendered electrode thickness of ≈142 μm after drying, whereby the three dryers were set to 55 °C, 70 °C, and 85 °C. The average weight fraction of the aluminum (wt%$_{alu}$) of the double-sided NCA electrodes is 12.6%. The NCA loading was chosen to yield the same cathode areal capacity of ≈2.3 mAh cm^{-2} at 1C as that which was achieved with the above specified LMR-NCM cathodes. The anodes were also coated double-sided at 0.5 m min^{-1} onto the same copper current collector foil. The average loading per side of the anodes used for the NCA/graphite cells is 10.2 ± 0.5 mg cm^{-2} (corresponding to ≈3.6 mAh cm^{-2}), resulting in an uncalendered electrode thickness of ≈222 μm for the anode electrodes dried as specified above.

Production step 3: calendaring.—The calender used for compaction was the EA 102 (Coatema, Germany) with a roll diameter of 400 mm and a maximum line-load of 1000 N mm^{-1}, at a constant roller speed of 0.5 m min^{-1} in all cases.[41] The thickness of the electrodes before and after calendering was measured with a tactile dial gauge (40 EWRi, Mahr, Germany). The electrode coating porosity ($\varepsilon_{coating}$) is 1 minus the ratio of the bulk volume of the electrode components (V_{solid}) over the volume of the coating ($V_{coating}$); the letter is determined by summing up the individual bulk volumes of the electrode components based on their bulk material density (ρ_i) and their relative weight fraction ($wt\%_i$) and dividing it by the coating area ($A_{coating}$) and the measured thickness of the coating ($d_{coating} = d_{electrode}$—$d_{current\text{-}collector}$) and finally multiplying this term by the total mass of the coating on both sides ($m_{coating}$):

$$\varepsilon_{coating} = 1 - \frac{V_{solid}}{V_{coating}} = 1 - \frac{\sum \frac{wt\%_i}{\rho_i}}{d_{coating} \times A_{coating}} \cdot m_{coating} \quad [1]$$

Since preliminary tests showed that calendering of the LMR-NCM cathodes turned out to be challenging (discussed in detail later), the influence of the process parameters roll pressure, compaction rate, and temperature of the calendering rolls were investigated. Based on an initial porosity of 56% ($\rho_{coating}$ = 1.74 g cm^{-3}), the roller temperatures of 25 °C, 40 °C, 60 °C, 90 °C, and 120 °C were investigated in a full factorial Design of Experiments (DoE) for the two targeted coating porosity values of 42% ($\rho_{coating}$ = 2.30 g cm^{-3}), and 32% ($\rho_{coating}$ = 2.69 g cm^{-3}). Based on laboratory coin cell tests and the achievable and processable densities of the electrodes, the final target porosity was set to 42% porosity ($\rho_{coating}$ = 2.30 g cm^{-3}), resulting in a compaction rate of ≈22% (from 167 μm to 131 μm thickness of the electrodes including two cathode coatings and one 15 μm aluminum foil). This was achieved by heating the calendering rolls to 120 °C to compact LMR-NCM electrodes for use in multilayer pouch cells.

The anodes were calendered from a pristine porosity of 55% ($\rho_{coating}$ = 1.00 g cm^{-3}) to a porosity of 30% ($\rho_{coating}$ = 1.55 g cm^{-3}) at 25 °C. This corresponds to a compaction rate of almost ≈35% (from 206 μm to 137 μm thickness of the electrodes including two anode coatings and one 11 μm copper foil).

Since preliminary tests have shown that calendering of the NCA electrodes is possible without heating the calendering rolls, NCA electrode calendering was performed based on the as-coated porosity

of 47% ($\rho_{coating}$ = 2.22 g cm^{-3}) to 42% ($\rho_{coating}$ = 2.43 g cm^{-3}) at 25 °C. Like the anodes for the LMR-NCM electrodes, the anodes for NCA were also calendered to 30% porosity ($\rho_{coating}$ = 1.55 g cm^{-3}).

Production step 4: vacuum drying (electrode coil).—The electrode coils were dried in a vacuum oven (TR03 LFC from Waldner Process Systems, Germany) for three alternating drying and vacuum cycles. Each drying cycle was carried out at a drying temperature of 120 °C and begins at ambient pressure in the dry room (dew point −40 °C) and includes the following evacuation cycle:p_{evac1} = 400 mbar, p_{evac2} = 200 mbar, p_{evac3} = 100 mbar, p_{evac4} = 50 mbar, p_{evac5} = 30 mbar, p_{evac6} = 20 mbar dwell time (t_{evac1} = 30 min, t_{evac2} =...= t_{evac6} = 5 min), and venting to ambient pressure level.

Production step 5: confectioning.—The separation of anode and cathode was performed by laser cutting with a cutting speed of 0.3 m min^{-1} and a laser power of 100 W. The used laser cutting module is a pulsed fiber laser (IGP Photonics, USA) with a wavelength of 1064 nm, a pulse width of 30 ns and a pulse frequency of 500 kHz.[33] The footprint of the anode coating of a thus cut electrode sheet is 104 mm · 76 mm (≡79.04 cm^2 anode coating) with a remaining uncoated current collector foil area of 67 mm · 15 mm (≡10.05 cm^2) for current conduction. The footprint of the cathode coating is 101 mm · 73 mm (≡73.73 cm^2 cathode coating), with the same size of uncoated substrate foil (≡10.05 cm^2) for current conduction.

Production step 6: stacking.—Both cell configurations (LMR-NCM/graphite and NCA/graphite) were stacked by z-folding with a configuration of 17 double-sided anode electrodes and 16 double-sided cathode electrodes using a celgard 2500 separator (Celgard LLC, USA) to obtain large-format multilayer pouch cells with an initial capacity at C/10 of 6.9 Ah for LMR-NCM (based on 27.6 g LMR-NCM in the cell and a nominal capacity of 250 mAh g^{-1}) and 6.1 Ah for NCA (based on 30.7 g NCA in the cell and a nominal capacity of 200 mAh g^{-1}). This results in a nominal cell energy of 24 Wh (LMR-NCM) and 23 Wh (NCA) based on averaged discharge voltages of 3.5 V for LMR-NCM cells and 3.7 V, for NCA cells respectively. The z-folding system was developed in cooperation with Manz Automation in a previous research project.[33]

Production step 7: contacting.—The substrate foils were initially contacted by ultrasonic welding in two steps with a Branson Ultraweld L20 system. For the LMR-NCM cathodes, the substrate foils were first contacted with an amplitude of 16 μm, welding energy of 180 J, and a clamping force of 124.11 kPa. Subsequently, the conductor tabs were joined to the welded substrate foils with the same parameters. For the NCA cathodes, the substrate foils were initially contacted with an amplitude of 16 μm, welding energy of 200 J, and a clamping force of 124.11 kPa. For contacting the tabs, the welding energy was reduced to 180 J.

For the anodes, both contacting steps were carried out with an amplitude of 20 μm, welding energy of 450 J, and a clamping force of 172.37 kPa.

Production step 8: packaging.—The cell stacks were packaged into a flexible pouch bag with a deep-drawn pocket. Three sides of the pouch foil were sealed with a linear sealing module (HH - 4424 003 from Harro Höflinger, Germany) using impulse sealing bars with the following parameters: 3 s sealing time, 3.50 bar sealing pressure, 195 °C sealing temperature, and a residence time of 1 s. One side of the pouch cell was left open for electrolyte filling.

Production step 9: vacuum drying (cell stack).—Prior to filling, the cells were dried in the same vacuum oven as in production step 4. The drying process was composed of four cycles with a drying temperature of 60 °C and includes six steps. Each cycle begins at ambient pressure in the dry room (dew point −40 °C) and includes the following evacuation sequence: p_{ev-1} = 400 mbar, p_{ev-2} = 200 mbar,

p_{ev-3} = 100 mbar, p_{ev-4} = 50 mbar, p_{ev-5} = 30 mbar, and p_{ev-6} = 20 mbar; the dwell time at each pressure setting was 30 min for the first step and 5 min for all subsequent steps, while in between each cycle the cell was vented to ambient pressure.

Production step 10: electrolyte filling.—For the LMR-NCM/graphite cells, a 1 M LiPF$_6$ electrolyte with 12 vol% FEC, 64 vol% DEC, 24 vol% of a proprietary co-solvent, and 2 wt% of a proprietary stabilizing additive was obtained from BASF. The proprietary additive improves full-cell cycle stability and has a similar effect as the one described in Guéguen et al.[54] The total amount of electrolyte added to LMR-NCM/graphite cells ($V_{electrolyte}$) was set to correspond to 1.5 times the total pore volume of electrodes and separator in the cell (V_{pores}); a value of ≈1.4–1.6 for this so-called volumetric factor ($V_{electrolyte}/V_{pores}$) was found to yield the highest capacity retention for NCM111/graphite multilayer pouch cells.[25] The thus calculated amount of electrolyte was 24.0 ml (or 31.2 g based on its density of 1.3 g ml^{-1}), corresponding to a $mass_{electrolyte}/mass_{CAM}$ of 1.1/1. Due to this small amount of electrolyte when compared to the void volume between the flexible pouch foil and the cell stack, a single electrolyte dosing step was selected. Therefore, the filling process was composed of six steps: flushing with inert gas, evacuation, dosing, sealing, venting, and wetting. The process was implemented by an automated filling station from Manz (Germany), whereby the 24.0 ml of electrolyte were dosed in a vacuum chamber at an absolute pressure of 80 mbar. The closing pressure of the sealing bars was set to 3 bar for 3 s, with a sealing temperature of 195 °C. After venting the vacuum chamber, the cells were left to wet for 4 h at 40 °C in a temperature chamber (LabEvent T7210/40/3, Vötsch, Germany) before formation.

For the NCA cells, the same volumetric factor of $V_{electrolyte}/V_{pores}$ = 1.5 and the same filling process was used as for the LMR-NCM cells. Here, however, a different electrolyte was used, namely 1 M LiPF$_6$ in a mixture of ethylene carbonate (EC) and diethyl carbonate (DEC) with a weight ratio of EC:DEC 3:7 plus 2 wt% vinylene carbonate (VC) (LP472, 1.2 g ml^{-1}, BASF). Thus, 23.0 ml of electrolyte (or 27.6 g based on its density of 1.2 g ml^{-1}) were added, corresponding to $mass_{electrolyte}/mass_{CAM}$ = 0.9/1.

After electrolyte filling and the final sealing of the cells, the mass of added electrolyte was also evaluated by determining the differences between the weight of the sealed cells and that of the cells prior to electrolyte filling. The thus determined electrolyte mass was lower by 10 ± 5% for the LMR-NCM/graphite cells and lower by 11 ± 1% for the NCA/graphite cells. This electrolyte mass deviation of ≈10% is likely caused by a system specific offset as well as electrolyte evaporation during the electrolyte filling at 80 mbar and the sealing process.

Production step 11: formation and degassing.—The formation of the cells was conducted after a 4 h rest period to allow for complete wetting of the electrodes and the separator. Cell cycling was conducted using a BaSyTec CTS system.

The LMR-NCM/graphite cells were initially charged in constant current (CC) mode with C/15 (referenced to a nominal capacity of 250 mAh/g$_{CAM}$) to 4.0 V at 40 °C. At 4.0 V, the cells were disconnected and degassed in the electrolyte filling station at 19 °C. For this purpose, the cells were opened by an automated knife (the size of the applied cut was 17 mm by 3 mm). Then the vacuum chamber was flushed with nitrogen and subsequently evacuated to 100 mbar, at which pressure the cells were resealed. After venting the system, the cells were electrically reconnected to the cell test system in the temperature chamber. After this first degassing step, the LMR-NCM/graphite cells were further charged at 40 °C in CC mode with C/15 to 4.7 V (0.1 V higher in this first activation cycle compared to the subsequent charge-discharge cycles, as is required for LMR-NCMs[23,55]) and then discharged in CC mode with C/15 to 4.0 V. At this point, a second degassing step was conducted, following the above given procedure. After this initial formation cycle at 40 °C, the cells were placed in a cell holder

where they are kept under a compression of ≈0.2 MPa (discussed in more detail in Part II of the paper[52]). Thereafter, the cells were placed in a temperature chamber controlled at 25 °C and discharged in CC mode with C/15 to 2.0 V; this was followed by two stabilization cycles in CC mode at C/10 between 2.0 V and 4.6 V.

The formation and degassing of the NCA/graphite cells was performed at 25 °C, Initially, the cells were charged at C/15 (referenced to a nominal capacity of 200 mAh/g$_{CAM}$) to an upper cut-off voltage of 4.3 V and then discharged to 4.0 V. At this point, the cells were degassed and re-sealed according to the above described procedure. Since there is very little gassing that originates from the NCA CAM compared to the LRM-NCM CAM (further details are provided in the Results and Discussion section), a single degassing step was sufficient for the NCA/graphite cells. Subsequently, the cells were placed in a cell holder where they were kept under a compression of ≈0.2 MPa and further discharged to 3.0 V at C/15. This was followed by two stabilization cycles at C/10 between 3.0 V and 4.3 V (all at 25 °C).

Preparation of coin cell based half-cells.— *Electrode preparation.—*The electrodes were produced using the same materials and electrode compositions as for the double-sided coated electrodes for the multilayer pouch cells. The electrode materials were mixed in a planetary mixer (Thinky Corp., USA) using the same sequential dilution procedure as described for the pouch cell electrodes, except that the solids contents of the final slurries were ≈4% lower. The slurries were coated onto the rough side of an aluminum current collector foil (15 μm thick, MTI, USA) with a box-type coating bar (Erichsen, Hemer, Germany), using an automated coater (RK PrintCoat Instruments, United Kingdom). Subsequently, they were dried in a convection oven at 50 °C for 5 h. The electrode coating loadings were varied by the gap size of the coater bar (120–400 μm wet film thickness) to achieve loadings between 6–21 mg$_{CAM}$ cm^{-2} after the drying step. The electrodes were calendered with a lab calender (Typ GK 300 L, Saueressig, Germany) to 42% or 32% electrode coating porosity.

*Coin cell assembly.—*For the coin cells, cathodes with 14 mm diameter were punched out from the single-side coated electrode sheets. Prior to cell assembly, the cathodes were dried in a glass oven (Büchi, Switzerland) under a dynamic vacuum at 120 °C for 12 h and then transferred into an argon-filled glove box (MBraun, Germany) without exposure to ambient atmosphere. The coin cells were assembled with two glass fiber separators (17 mm diameter, glass microfiber filter 691, VWR, Germany) that were wetted with 100 μl of the same electrolytes as those used for the pouch cells (i.e., the FEC based electrolyte for coin cells with LMR-NCM and the LP472 electrolyte for those with NCA). For all coin cell tests, the counter-electrode was a lithium metal disk (15 mm diameter, 450 μm thick, 99.9%, Rockwood Lithium).

*Coin cell cycling.—*All coin cell tests were performed with a Maccor cycler (series 4000, USA) and with the cells placed in a temperature-controlled chamber at 25 °C.

The lower cut-off potential for the LMR-NCM/lithium half-cells were set to 2.0 V. The upper cut-off potential is set to 4.8 V in the first activation cycle (i.e., 0.1 V higher than in the case of LMR-NCM/graphite cells to obtain the same upper cut-off value for the cathode electrode) that was conducted in CC mode at C/15 (referenced to 250 mAh/g$_{CAM}$); different from the pouch cells, the activation cycle for LMR-NCM/lithium coin cells was conducted at 25 °C (as discussed later, the 40 °C activation was only necessary for pouch cell to address the strong gassing in the activation cycle). The two following stabilization cycles were conducted at C/10 (CC) between 2.0 V and 4.7 V.

The NCA/lithium cells were cycled at 25 °C between 3.0 and 4.4 V. The first formation cycle was performed in CC mode at C/15 (referenced to 200 mAh/g$_{CAM}$). The following two stabilization cycles were carried out at C/10 between the same voltage limits.

After cell formation/stabilization, discharge rate capability tests were conducted. In these tests, the cells were always charged at C/2 followed by a CV (constant voltage) phase until the current decreased to below C/20. The following discharge rates were applied in CC mode: C/2 (3 cycles), 1C (5 cycles), 3 C (10 cycles), and finally C/2 again (8 cycles).

Ex-situ and operando characterization methods.— *Mercury intrusion.—*PoroTec GmbH performed the Mercury porosimetry measurements with the Mercury intrusion porosimeters Pascal 140 and Pascal 440 from ThermoFisher Scientific. The measurements were performed with a penetrometer of 7.4 ml bulb volume and 0.5 ml stem volume. In order to examine a representative sample volume, a sample weight of ≈1–1.5 g (=15–25 pieces of ≈2–2.5 cm^2 double-side coated electrode pieces) was added to the penetrometer. To obtain statistically significant results, three independent measurements each were taken for the as-coated LMR-NCM (porosity of 56%) and NCA (porosity of 47%) cathodes, as well as for the calendered LMR-NCM and NCA cathodes with porosities of 42% and 32%. By averaging at least three measured values and indicating the standard deviation, it can be ensured that for each porosity level a representative section of the electrode is evaluated by mercury porosimetry. The measured pore diameter (*D*) correlates with the pressure (*P*) required for intrusion of mercury through the Washburn equation (Eq. 2):

$$D = -\frac{4\gamma \cos(\theta)}{P} \qquad [2]$$

Data analysis was based on a constant contact angle (*θ*) of 140° and constant surface tension (*γ*) of 0.48 N m^{-1} for mercury. The data were measured within a pressure range of 0–400 MPa, corresponding to pores down to a diameter of ≈3 nm. The measurements were corrected by a blank measurement of the empty penetrometer, and the compressibility of the individual electrode materials was considered negligible.

For the contribution of the conductive carbon black additive, supplementary measurements were performed with the MicroActive AutoPore V 9600, using a contact angle of 140 °. To evaluate the carbon black (CB) contribution, CB-only electrodes (66.7/33.3 wt% CB/PVdF and a CB loading of ≈2.5 mg cm^{-2}) and electrodes consisting of NCA without CB (96.5/3.5 wt% NCA/PVdF with an NCA loading of ≈18 mg cm^{-2}) were measured both uncalendered and calendered. A penetrometer with a 5.0 ml bulb and 0.4 ml stem volume was used for these samples. A sample mass of about 0.8 g was used for the NCA coatings without CB to obtain a constant ratio of sample mass to bulb volume of ≈0.2 g ml^{-1}, using ≈25 pieces of ≈1.0 cm · 1.5 cm single-side coated electrodes. For the CB-only coating the same number of single-side coated pieces (≈25) as for the NCA coating without carbon black was used.

*Nitrogen physisorption analysis.—*Surface area and pore volume measurements were performed on a gas sorption analyzer (Autosorb-iQ, Quantachrome, USA) at −196.15 °C using nitrogen as adsorbent. Beforehand, the pristine powders were degassed under vacuum at 120 °C for 12 h. The specific surface area was determined from adsorption isotherms in the relative pressure range of 0.008 < p/p$_0$ < 0.25 according to the Brunauer-Emmet-Teller (BET) theory. The specific total pore volume of adsorbed nitrogen can be determined at the limiting pressure p/p$_0$ ⩾ 0.986 of the adsorption branch and therefore includes pore volumes up to ≈ 140 nm. The pore volume (*V$_{pore}$*) can be calculated with the volume of nitrogen adsorbed (*V$_{ads}$*) using Eq. 3:

$$V_{pore} = \frac{P * V_{ads} * V_m}{RT} \qquad [3]$$

where *P* is the pressure, *V$_m$* the molar volume of nitrogen at −196.15 °C (i.e., 34.7 cm^3 mol^{-1}), *R* the universal gas constant, and *T* the temperature.

Particle size determination.—The size of the secondary agglomerates were determined by dispersing the particles in ethanol and then using laser scattering (LA-950V2, Horiba, Japan); the data were analyzed by means of the Mie scattering theory.

SEM cross-sectional imaging.—The electrodes were placed between a z-folded carbon paper (H1410–14, Freudenberg, Germany) that was compressed between two aluminum plates (1.0 cm · 1.0 cm · 0.1 cm). The electrodes were then imbibed by a liquid epoxy resin (EpoThin 2, Buehler, Switzerland): with the resin still liquid, the sample stack was placed into a desiccator, which was then evacuated to ensure complete filling of the pores by the resin. After the resin had hardened, the sample stack was polished with SiC paper (CarbiMet S, P320, Buehler, Switzerland) until the electrode cross-section was fully exposed. Afterward, the electrode was polished using a finer SiC paper (CarbiMetS, P1200, Buehler, Switzerland) and a diamond based polishing suspension (MetaDiSupreme, Polycrystalline Diamond Suspension, 9 μm, Buehler, Switzerland). The final polishing step was performed using a 50 nm Al_2O_3 agent (MasterPrep Alumina Suspension, Buehler, Switzerland) on a micro cloth (ChemoMet, Buehler, Switzerland). The scanning electron microscopy (SEM) images were acquired using a Jeol JSM-7500F field emission SEM at 1 kV with an LEI detector and a magnification of 1000.

OEMS measurements.—The LMR-NCM slurry to prepare electrodes for on-line electrochemical mass spectrometry (OEMS) was prepared as described above (92.5/4/3.5 wt% CAM/CB/PVdF) and coated with a wet film thickness of 20 μm onto a stainless-steel mesh (SS316, aperture 26 μm, wire diameter 25 μm, The Mesh Company, UK), yielding a LMR-NCM loading of 12–14 mg cm^{-2} (3–3.5 mAh cm^{-2} based on 250 mAh/g$_{CAM}$). In this case, the electrodes for were punched out with a diameter of 15 mm and compressed for 20 s with 2 t to yield a porosity of $\approx$45%. For the anode side, the same graphite electrode sheet as prepared for the pouch cells was used and punched out with a diameter of 17 mm. The electrodes were dried together with a glass fiber separator of 24 mm diameter in a glass oven (Büchi, Switzerland) under a dynamic vacuum at 120 °C for 12 h and then transferred into an argon-filled glove box without exposure to the atmosphere.

For OEMS measurements, a custom-made cell was used; the specific cell design as well as the OEMS setup were previously published.[50] OEMS cells were assembled with the graphite anode placed onto the bottom part of the OEMS cell, followed by the glass fiber separator soaked with 300 μl of the FEC/DEC based LMR-NCM electrolyte that was used for the coin and multilayer pouch cells. The mesh-supported LMR-NCM cathode was placed on top of the separator and is thus located just below the flow-restricting capillary that leads to the mass spectrometer. The cells were connected to the mass spectrometer, held for 4 h at OCV (open circuit voltage), and were then charged to 4.7 V at a C/12 rate with a final CV phase until a cut-off current of C/24, followed by a discharge to 2.0 V at C/12. After this first activation cycle, the cells were flushed for 2 min with argon to re-pressurize the cell (over the $\approx$24 h long activation cycle, $\approx$1.5 ml of the 11 ml gas head-space of the OEMS cell are leaked into vacuum through the flow-restricting capillary with a specified leak rate of $\approx$1 μl min^{-1}). The cell was then stabilized for 4 h at OCV, followed by three cycles at C/4 between 2.0–4.6 V with a CV phase at 4.6 V until a cut-off current of C/8.

To quantify the mass spectrometer signals, a calibration gas containing H_2, O_2, CO_2, and CO (each 2000 ppm) in argon (Linde AG, Germany) was used. All mass spectrometer signals were normalized to the signal at a mass-to-charge ratio m/z = 36 (corresponding to the 36 Ar isotope) to correct for minor variations in cell pressure and temperature. Afterward, the signals at m/z = 44 (CO_2), m/z = 32 (O_2), m/z = 2 (H_2), and m/z = 28 (CO) were converted into a gas concentration using the ideal gas law, taking a

gas head-space volume of the OEMS cell of roughly 11 ml into consideration.

Large-format cell energy density projections from coin cell data.—The measured half-cell performance in coin cells with the different cathode active materials was utilized to project the performance of large-format multilayer pouch cells with a cell stack configuration of 17/16 double-side coated anode/cathode sheets. The *cell configuration tool* (see Excel file in the supporting information) considers the weight of all inactive cell components (current collector foils and tabs, pouch cell foil), the geometrical overlap of the anodes, the weight of the electrolyte based on the volumetric factor of $V_{electrolyte}/V_{pores}$ (1.5 for the multilayer pouch cells built here), and the separator. The Excel-based tool is designed to project the full-cell multilayer pouch cell energy density based on half-cell coin cell data. For this, the half-cell data are corrected by the 0.1 V lower upper cut-off voltage in CAM/graphite full-cells compared to CAM/lithium half-cells as well as by the smaller capacity of full-cells due to the first-cycle irreversible capacity loss. This loss is either dominated by the SEI loss of the anode or by the cathode first-cycle efficiency (most often the case for NCM based cathodes). The first-cycle efficiency is slightly reduced for the CAM/graphite full-cells compared to CAM/lithium half-cells (by $\approx$9 mAh/g$_{CAM}$), because in this work the lower voltage cut-off in full-cells was chosen to be the same as for half-cells, so that the CAM is slightly less discharged in the full-cells as in the corresponding half-cells.

Results and Discussion

LMR-NCM electrode design based on LMR-NCM/Lithium half-cells.— *Loading dependent discharge rate capability.*—To the best of our knowledge, there is only one study in the literature on the rate capability of LMR-NCM cathodes as a function of loading.[56] Since this relation strongly depends on the individual LMR-NCM material composition and morphology, preliminary investigations were performed with LMR-NCM/lithium half-cells at the coin cell level (Fig. 2). For this purpose, LMR-NCM cathodes with four different loadings were prepared on a laboratory scale, calendered to 42% porosity, and subjected to a rate capability test (see Experimental section).

Already at the two stabilization cycles at C/10 (cycles 2 and 3), the electrodes with the highest LMR-NCM loading of $\approx$21.1 mg cm^{-2} ($\equiv$5.3 mAh cm^{-2} based on a nominal capacity of 250 mAh/g$_{CAM}$) show a significantly lower specific discharge capacity than the electrodes with the lower LRM-NCM loadings of $\approx$15.3 mg cm^{-2} ($\equiv$3.8 mAh cm^{-2}), of $\approx$11.4 mg cm^{-2} ($\equiv$2.9 mAh cm^{-2}), and of $\approx$6.9 mg cm^{-2} ($\equiv$1.7 mAh cm^{-2}) which all reach about the same specific capacity of $\approx$250 mAh/g$_{CAM}$ (see Fig. 2). This effect is even more apparent at a discharge rate of C/2 (cycles 4–6) and 1C (cycles 7–11), where the three lower loadings still yield essentially identical discharge capacities (e.g., $\approx$200 mAh/g$_{CAM}$ at 1C), which are much higher than those observed for the LMR-NCM electrodes with the highest loading of $\approx$21.1 mg cm^{-2} (e.g., only $\approx$125 mAh/g$_{CAM}$ at 1C). At 3C (cycles 12–21), the specific discharge capacity not only decreases significantly for all LRM-NCM loadings, but now also shows a clear trend of decreasing specific discharge capacity with increasing loading. In the C/2 cycles after the ten cycles at 3C (i.e., cycles 22–29), the specific discharge capacity of all the cells is essentially identical with that recorded in the initial C/2 cycles (cycles 4–6), with $\approx$225 mAh/g$_{CAM}$ for the three lowest loadings and $\approx$180 mAh/g$_{CAM}$ for the highest loading. This retention of the capacity shows that the capacity loss at high C-rates must have been caused mainly by the high concentration overpotentials at high C-rates, which are more pronounced for the high-loaded cathodes, as they are both thicker and are operated at higher geometric current densities (at 3C, e.g., the geometric current densities increase from $\approx$5.1 mA cm^{-2} for the $\approx$6.9 mg cm^{-2} electrodes with a thickness of $\approx$33 μm to $\approx$15.9 mA cm^{-2} for the
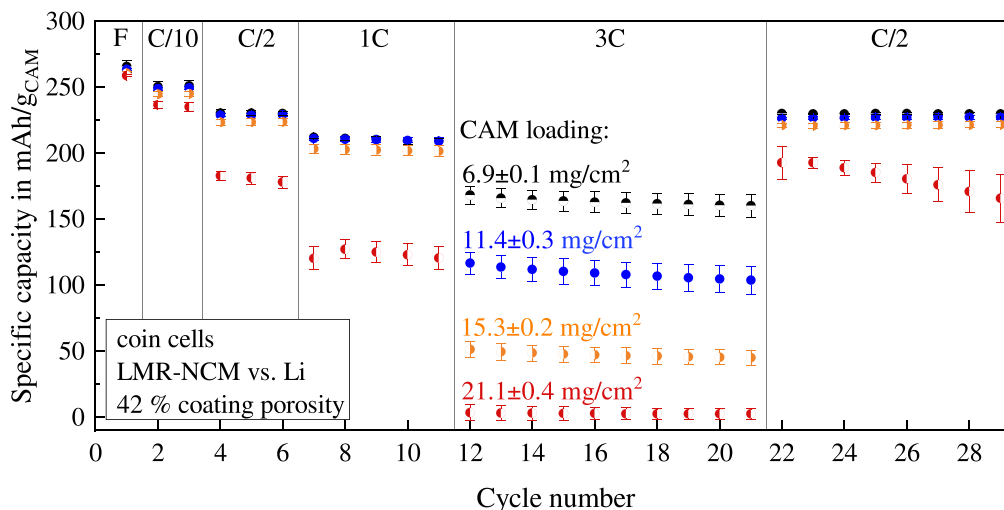
Figure 2. Discharge rate capability test at 25 °C of LMR-NCM/lithium coin cells with different LMR-NCM loadings (calendered to a porosity of 42%) after a first-cycle activation at C/15 (CC) between 2.0 V and 4.8 V (referred to as F for formation) and two CC stabilization cycles between 2.0 V and 4.7 V at C/10 (C-rates are referenced to a nominal specific capacity of 250 mAh/g_{CAM}). The subsequent cycles are conducted between 2.0 V and 4.7 V at different discharge rates (C/2, 1C, 3C, and C/2, all in CC mode) and with a CC charge at C/2 followed by a CV phase until the current decreased to below C/20. The CAM loadings indicated in the figure represent the average and the standard deviation of three individual cells (except for the ≈15 mg cm^{-2} electrodes, for which only two cells were tested). The capacity data for each CAM loading series were averaged over three independent cells (two in case of the ≈15 mg cm^{-2} electrodes), with the standard deviation as error bars. The FEC/DEC based electrolyte specified in the Experimental section was used.

≈21.1 mg cm^{-2} electrodes with a thickness of ≈107 μm). While for the electrodes with an LRM-NCM loading of ≈21.1 mg cm^{-2} some capacity fading appears to occur toward the end of this rate capability test at C/2 (cycles 22–28), this must not necessarily reflect a degradation of the cathode active material but may be due to a degradation of the metallic lithium anode at the high current densities required for electrodes with such high areal capacities. Thus, meaningful CAM cycle-life tests must be conducted in full-cells rather than half-cells,[57] and LMR-NCM/graphite cycle-life tests with multilayer pouch cells with a nominal areal capacity of ≈2.9 mAh cm^{-2} are presented in Part II of this work.[52]

As discussed in the literature, the energy density of large-format battery cells is primarily a function of the active material loadings and also of the electrode thickness, whereas the rate capability in general decreases for higher active material loadings.[58] Therefore, there is a sweet spot for maximizing the energy density of large-format cells for a given C-rate requirement. For small-scale laboratory cells, energy density is generally not considered and to obtain the best C-rate performance when testing new cathode active materials, rather low CAM loadings are usually used, as is the case for many studies with LMR-NCM cathode active materials.[10,19–22,46] However, as we will demonstrate in the following, small-scale half-cell tests with different CAM loadings can be used to project the performance and energy density of large-format full-cells.

Table I lists the specific discharge (DCH) capacities, the corresponding discharge voltages, and CAM based energy densities obtained from the LMR-NCM/lithium coin cell experiments at C/10, 1C, and 3C for the four different LMR-NCM loadings shown in Fig. 2. These LMR-NCM performance characteristics determined in half-cells cells were then used to project the performance and energy density of large-format cells with a cell stack configuration of 17/16 double-side coated anode/cathode sheets that were used to construct ≈6.9 Ah (at C/10) multilayer pouch cells, considering the mass of all inactive components (current collector foils and tabs, pouch cell foil), the electrolyte (for $V_{electrolyte}/V_{pores} = 1.5$), and the separator, as specified in the Excel-based calculation tool (see *cell configuration tool* in the supporting information). To project the large-format multilayer pouch cell energy densities, the mean discharge voltages from the half-cell measurements were reduced by 0.1 V, accounting for the higher potential of the graphite anodes used in a full cell setup. Furthermore we reduced the half-cell capacity according to

the first cycle irreversible losses (i.e., by 9 mAh/g_{CAM}; see Experimental section).

As can be seen in Table I, the measured specific energy densities on the CAM level (in units of mWh/g_{CAM} and referenced to the lithium potential) decrease with increasing LRM-NCM loadings, independent of the applied C-rate. Since the smaller loadings have only a slightly higher discharge capacity and voltage for C/10, the energy density at the cell level rises with increasing LMR-NCM loadings from 168 Wh/kg_{cell} (for ≈6.9 mg cm^{-2}) to 222 Wh/kg_{cell} (for ≈21.1 mg cm^{-2}). In contrast, the strong decrease in capacity and discharge voltage drop at 3C for high LMR-NCM loadings results in higher energy densities on the cell level for the smaller loadings. For a C-rate of 1C, the highest energy density on the cell level can be found for the intermediate loadings of ≈11.4 and ≈15.3 mg cm^{-2}, reaching 159–162 Wh/kg_{cell}. In Table I, the LMR-NCM loadings that yield the highest cell level energy density at a given C-rate are highlighted (15.3 and 21.1 mg cm^{-2} for C/10, 11.4 and 15.3 mg cm^{-2} for 1C and 6.9 mg cm^{-2} for 3C). As the multilayer pouch cells produced within this work are targeted to operate up to a maximum C-rate of 1C, an LMR-NCM loading of ≈12 mg cm^{-2} was chosen for the multilayer pouch cells.

Porosity dependent discharge rate capability.—Based on the above findings, the loading of ≈12 mg cm^{-2} for LMR-NCM/lithium coin cells (corresponding to a nominal areal capacity of ≈3.0 mAh cm^{-2} at 0.1C) was selected to investigate different coating densities in the next step. For comparison, NCA/lithium coin cells with a similar areal capacity of ≈2.7 mAh cm^{-2} (≈13.5 mg cm^{-2} NCA loading) were examined also. To determine the influence of calendering on the C-rate performance, the LMR-NCM, as well as the NCA cathodes, were calendered to two porosity levels (42% and 32%) from the as-coated (uncalendered) porosities of 56% and 47%, respectively. The results of the rate capability test conducted in the same way as that described in Fig. 2 is shown in Fig. 3.

The results of the discharge rate capability test with different cathode porosity levels (Fig. 3) show that, except for 3C, the cathode coating porosity within the considered range (i.e., from 56% to 32% for the LMR-NCM cathodes and from 47% to 32% for the NCA cathodes) has a negligible influence on the C-rate performance. Thus, it can be concluded that the cathode porosity does not have a large impact on the achievable capacity until rather high C-rates for

Table I. Impact of cathodes with different CAM loadings (calendered to a porosity of 42%) based on the LRM-NCM/lithium coin cell data in Fig. 2 (always using the 2nd cycle for each C-rate) on the materials level LMR-NCM performance characteristics and on the projected energy density for multilayer pouch cells with a nominal capacity of ≈6.9 Ah (at 0.1C). The latter is based on the Excel-based projection tool provided in the supporting information (referred to as cell configuration tool). The given values are averaged over three individual coin cells for each LMR-NCM loading (two in case of the 15.3 mg cm^{-2} loading).

Coin cell data & energy density	C-rate	CAM loading in mg cm^{-2}/areal capacity at 0.1C inmAh cm^{-2}			
		6.9 ± 0.1/≈1.7	11.4 ± 0.3/≈2.9	15.3 ± 0.2/≈3.8	21.1 ± 0.4/≈5.3
DCH capacity in mAh/g$_{CAM}$	C/10	251 ± 4	250 ± 1	245 ± 1	238 ± 3
avg. half-cell DCH voltage in V	C/10	3.640 ± 0.004	3.638 ± 0.002	3.633 ± 0.003	3.56 ± 0.01
CAM spec. energy in mWh/g$_{CAM}$	C/10	914 ± 1	908 ± 1	891 ± 1	848 ± 3
cell spec. energy in Wh/kg$_{cell}$[a]	C/10	168	202	216	**222**
DCH capacity in mAh/g$_{CAM}$	1C	212 ± 1	211 ± 2	203 ± 3	120 ± 7
avg. half-cell DCH voltage in V	1C	3.50 ± 0.01	3.42 ± 0.04	3.33 ± 0.02	2.83 ± 0.08
CAM spec. energy in mWh/g$_{CAM}$	1C	743 ± 1	723 ± 2	676 ± 3	341 ± 7
cell spec. energy in Wh/kg$_{cell}$[a]	1C	135	**159**	**162**	85
DCH capacity in mAh/g$_{CAM}$	3C	166 ± 7	114 ± 9	50 ± 4	3 ± 5
avg. half-cell DCH voltage in V	3C	3.30 ± 0.03	3.1 ± 0.1	2.93 ± 0.06	2.2 ± 0.1
CAM spec. energy in mWh/g$_{CAM}$	3C	552 ± 7	353 ± 9	145 ± 4	7 ± 5
cell spec. energy in Wh/kg$_{cell}$[a]	3C	**98**	75	30	n.a.

a) Calculated with the Excel-based projection tool (see *cell configuration tool* in the supporting information) using the here listed performance characteristics of LMR-NCM/lithium coin cells with different LMR-NCM loadings (using the average loading values). The essential assumptions are: i) 17/16 double-side coated anode/cathode sheets (89.09/83.78 cm^2 for anode/cathode sheet); ii) anode coating porosity of 30%; iii) anode/cathode active areas of 79.04/73.73 cm^2; with an areal capacity ratio of 1.2/1; iv) Al/Cu current collector thickness of 15/11 μm; v) Celgard 2500 separator (25 μm thick, 55% porosity); vi) electrolyte volume determined by $V_{electrolyte}/V_{pores}$ = 1.5; vii) LMR-NCM/graphite full-cell voltages are assumed to be 0.1 V lower than the here listed half-cell voltages and 9 mAh g^{-1} lower than the here listed half-cell capacities. All further specifications like current collector tab size/mass, pouch foil mass, etc., are specified in the Excel-based *configuration tool*.
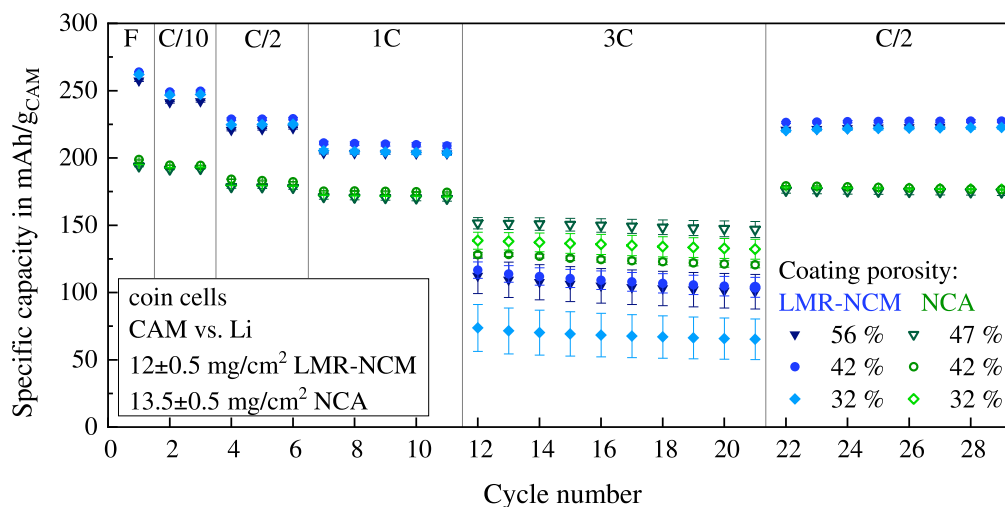

Figure 3. Discharge rate capability test at 25 °C of LMR-NCM/lithium and NCA/lithium coin cells with different cathode coating porosities, either as-coated, resulting in 56% and 47% porosity for LMR-NCM and NCA, respectively, or calendered to 42% and 32% (porosities are calculated based on Eq. 1 and are within an accuracy of ±2 percentage points). For LMR-NCM/lithium cells, the formation, stabilization, and further cycling were conducted as described in Fig. 2 (C-rates referenced to 250 mAh/g$_{CAM}$); NCA/lithium coin cells were cycled between 3.0 V and 4.4 V (C-rates referenced to 200 mAh/g$_{CAM}$), but otherwise followed the same procedure. The NCA loadings are 13.5 ± 0.5 mg cm^{-2} (≡2.7 mAh cm^{-2} at 0.1C) and the LMR-NCM loadings are 12 ± 0.5 mg cm^{-2} (≡3 mAh cm^{-2} at 0.1C). The shown data points are averaged over three independent cells per porosity (only two for the cells with the 32% porosity LMR-NCM coating), with the standard deviation as error bars.

moderately low porosities of 32%. However, as illustrated in Table II, cathode porosity has a significant impact on the gravimetric and volumetric energy density on a cell level. While the volumetric density change is obvious and follows directly from the decrease of electrode thickness with decreasing cathode porosity, the gravimetric cell energy densities also decrease with decreasing porosity on account of the thus reduced electrolyte volume and mass when maintaining the volumetric factor at $V_{electrolyte}/V_{pores}$ = 1.5.

The energy densities in Table II show that low LMR-NCM cathode porosities work well on the materials level. The predicted performance at the cell level (done with the *cell configuration tool* in

the supporting information), illustrates the importance of calendering on the cell level specific and volumetric energy density, while having a rather negligible effect on the rate capability up to 1C (see Fig. 3): the cell level specific energy density increases by up to 13%, while the gravimetric energy density increases by up to 18% (actually projected values are given for 0.1C in Table II, but the percentage increase is valid up to 1C).

As will be shown in the next section, calendering of large-scale LMR-NCM cathode coatings to porosities of 32% is not feasible, so that a porosity of 42% was targeted for the final large-scale production of LMR-NCM electrodes and thus for the production

Table II. Impact of the cathode porosities on the performance of LMR-NCM/lithium coin cells at C/10 (using the 2nd C/10 cycle of the discharge rate capability test shown in Fig. 3) on the materials level LMR-NCM performance characteristics and on the predicted energy densities (based on the cell configuration tool given in the supporting information) for a nominal 6.9 Ah pouch cells. Here, the LMR-NCM loadings are 12 ± 0.5 mg cm^{-2} ($\equiv$3 mAh cm^{-2} at 0.1C), the given values are averaged over three individual coin cells for each LMR-NCM cathode porosity (only two in case of the 32% porosity), stating the average values and their standard deviations. The values for an NCA cathode calendered to 42% porosity and based on the NCA/lithium coin cell data shown in Fig. 3 are given for comparison (for NCA loadings of 13.5 ± 0.5 mg cm^{-2}, corresponding to $\equiv$2.7 mAh cm^{-2} at 0.1C).

Coin cell data & energy density at C/10	Cathode porosity			
	LMR-NCM 56%	LMR-NCM 42%	LMR-NCM 32%	NCA 42%
DCH capacity in mAh/g$_{CAM}$	242 ± 1	250 ± 1	247 ± 1	197.1 ± 0.5
DCH half-cell voltage in V	3.637 ± 0.001	3.638 ± 0.002	3.636 ± 0.001	3.827 ± 0.001
CAM spec. energy in mWh/g$_{CAM}$	880 ± 1 ($\equiv$100%)	909 ± 1 (=103%)	898 ± 1 (=102%)	754.3 ± 0.5
cell spec. energy in Wh/kg$_{cell}$[a)]	186 ($\equiv$100%)	206 (111%)	210 (=113%)	193
cell grav. energy density in Wh/l$_{cell}$[a)]	402 ($\equiv$100%)	459 (=114%)	475 (=118%)	433

a) Calculated with the Excel-based projection tool (see *cell configuration tool* in the supporting information) using the here listed performance characteristics of LMR-NCM/lithium and NCA/lithium coin cells (using the average loading values). The essential assumptions are: i) 17/16 double-side coated anode/cathode sheets (89.09/83.78 cm^2 for anode/cathode sheet); ii) anode coating porosity of 30%; iii) anode/cathode active areas of 79.04/73.73 cm^2; with an areal capacity ratio of 1.2/1; iv) Al/Cu current collector thickness of 15/11 μm; v) Celgard C2500 separator (25 μm thick, 55% porosity); vi) electrolyte volume determined by $V_{electrolyte}/V_{pores}$ = 1.5; vii) LMR-NCM/graphite full-cell voltages are assumed to be 0.1 V lower than the here listed half-cell voltages. All further specifications like current collector tab size/mass, pouch foil mass, etc., are specified in the Excel-based *configuration tool*.

of large-format multilayer LMR-NCM/graphite pouch cells. In order to provide a meaningful comparison between LMR-NCM/graphite and NCA/graphite large-format cells, the NCA cathode coatings were also calendered to a porosity of 42%, even though the large-scale production of NCA cathode coatings with the lower porosity of 32% would be possible without problems.

Effect of the CAM morphology on the calendering process.—
Calendering process.—The LMR-NCM coating was initially calendered to 42% porosity, a compaction degree that is usually unproblematic for cathode active materials. Figure 4a shows a side view of the calendered electrode (with calendering rolls at 25 °C) coated double-sided with LMR-NCM cathodes before rewinding the electrode to the coil, and Fig. 4b provides a zoomed-in view as well as a representative top view of this electrode. The clearly apparent embossing of the aluminum foil at the coating edge[42] was unexpected for this still rather high porosity of 42% and is not observed for electrodes coated on both sides with NCA cathodes that were also calendered to the same final porosity of 42% with calendering rolls at 25 °C (see Fig. 4c). As will be shown later, this effect is due to the different morphology of the LMR-NCM CAM compared to the NCA CAM. To minimize the embossing of the aluminum foil in the case of the LMR-NCM electrodes, the calendering rolls were heated, which allowed a lowering of the calendering line-load,[41] and thus reduced the extent and number of electrode defects.[42]

Despite calendering to a moderate porosity of 42%, the LMR-NCM electrodes have a pronounced bowl-shape geometry and show strong aluminum foil embossing for the standard calendering procedure (a rolling speed of 0.5 m min^{-1}, and calendering rolls at 25 °C, as was used for NCA electrodes), which by GÜNTHER et al.[42] is ascribed to embrittlement for highly compressed cathode materials. Any further processing in the pilot scale production line of electrodes with these severe defects is not possible, because automatic processes for example electrode transport and alignment with vacuum grippers or exact laser cutting require flat and uniform surfaces. A hypothesis to explain this behavior is that the LMR-NCM cathode must have little elastic deformation and is thus also sensitive to current collector foil tears during further processing. The best calendering results for the LMR-NCM electrodes could be achieved with calendering rolls heated to 120 °C (please note that the images shown in Figs. 4a and 4b are for the non-optimized calendering process with calendering rolls at 25 °C).

On the other hand, the NCA electrodes proved to be less sensitive to calendering to 42% porosity and any subsequent processing steps

were unproblematic, so that the standard calendering procedures with calendering rolls at 25 °C could be used.

Cross-sectional SEM image analysis.—LMR-NCM (Figs. 5a–5c) and NCA (Figs. 5d–5f) electrodes compacted to the different porosity levels (calculated according to Eq. 1) are shown by cross-sectional SEM images. In addition to the different coating thicknesses from which the porosities were calculated (Eq. 1), these images show the respective agglomerate packing densities and morphologies of the LMR-NCM and NCA electrode coatings.

Comparing the SEM images of the uncalendered LMR-NCM (Fig. 5a) and NCA cathodes (Fig. 5d) cathodes, the packing density of the particles appears comparable, even though the overall cathode porosity of these uncalendered electrodes varies from 47% for the NCA to 56% for the LMR-NCM cathodes. On the other hand, after calendering the LMR-NCM and NCA electrodes to the same overall cathode porosity of either 42% or 32% (calculated according to Eq. 1), the individual LMR-NCM particles appear more densely packed (see Figs. 5b and 5c) compared to the NCA particles (see Figs. 5e and 5f). The porosity values determined by measuring the electrode thickness with a tactile dial gauge agree within 2 percentage points with the porosity determined by measuring the cathode thickness from the SEM images, confirming that the here specified overall porosity values are reliable. Nevertheless, a visual comparison of the cross-sections of the two different cathodes calendered to the same porosity (either 42% or 32%) indicates a larger apparent pore volume in the NCA cathodes compared to the LMR-NCM cathodes. This suggests that there must be an additional internal, optically "hidden" porosity within the here imaged LMR-NCM particles, i.e., within the secondary agglomerates of the LMR-NCM particles.

More detailed SEM images reveal that the large secondary agglomerates are composed of primary particles, as was already shown in the literature for NCA[59,60] and LMR-NCM[20,61] CAMs. For the here used materials, the primary particles of LMR-NCM are much smaller ($\approx$0.05–0.2 μm) than the primary particles of NCA ($\approx$0.2–2 μm). Furthermore, laser scattering analysis shows that the secondary agglomerates of the LMR-NCM material have a smaller d$_{50}$ diameter of $\approx$10 μm compared to $\approx$15 μm sized secondary agglomerates of the NCA material, which is in qualitative agreement with the SEM cross-sections shown in Figs. 5a and 5d. Since the targeted overall porosity for the calendering process based on Eq. 1 does not distinguish between porosity *between* secondary agglomerates and *within* secondary agglomerates, the secondary particles of
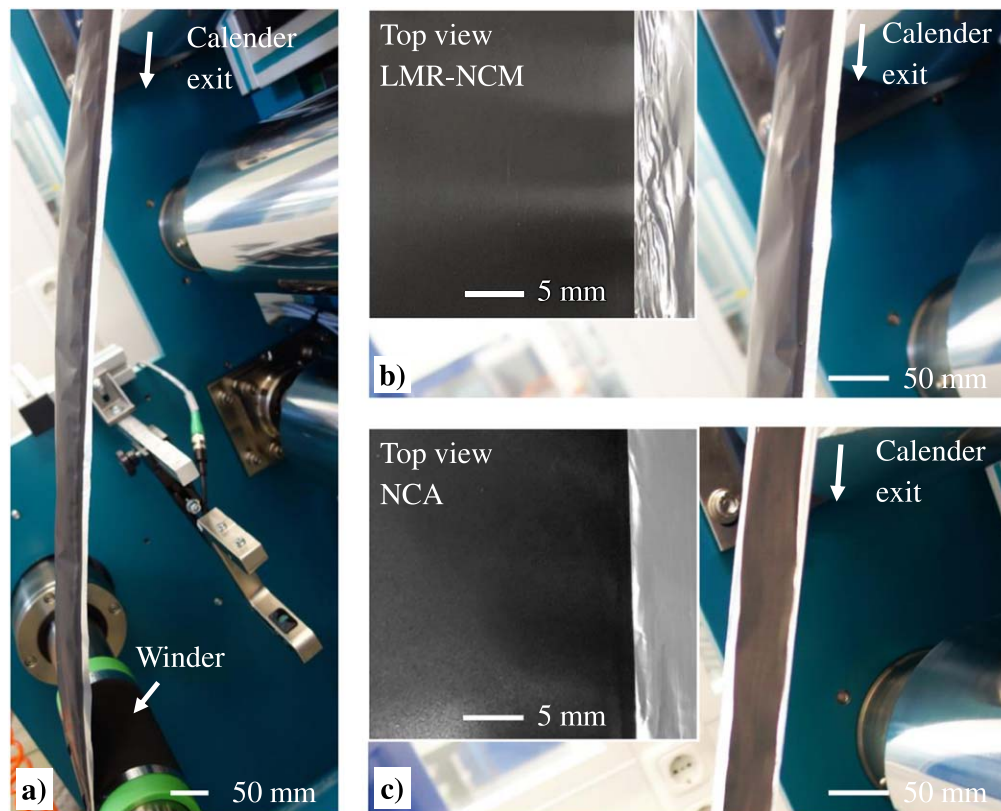
Figure 4. (a) Side view of an electrode coated on both sides with LMR-NCM cathodes after calendering to a porosity of 42% (2.32 g cm^{-3}); (b) zoomed-in side view as well as top view. (c) Zoomed-in side view as well as top view of an electrode coated on both sides with NCA cathodes after calendering to 42% porosity (2.45 g cm^{-3}). Both electrodes were calendered with the calender EA 102 from Coatema, with a roll diameter of 400 mm and a roller temperature of 25 °C. The depicted side views show the electrodes after the first deflection-roll downstream from the calender gap and in front of the winder.
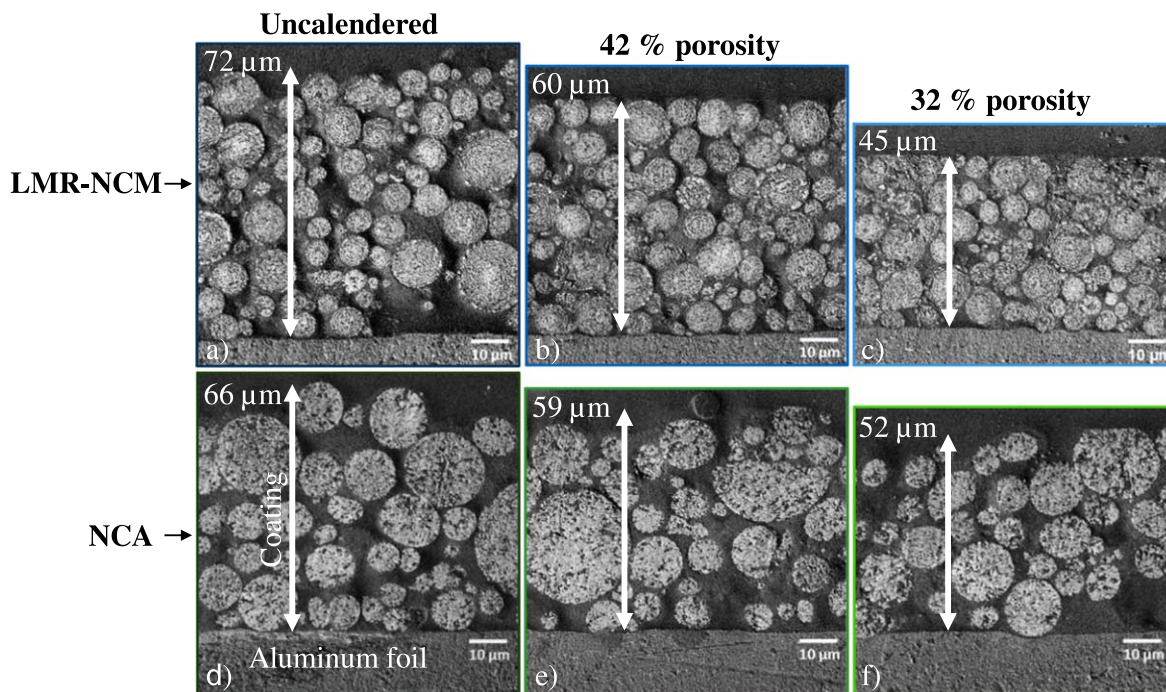

Figure 5. SEM cross-sectional images of as-coated and calendered electrodes (for preparation of the cross-sections see SEM cross-sectional imaging in the Experimental section). <u>First row</u>: LMR-NCM cathodes (a) uncalendered (with 56% porosity) or calendered to (b) 42% porosity or (c) 32% porosity. <u>Second row</u>: NCA cathodes (d) uncalendered (with 47% porosity) or calendered to (e) 42% porosity or (f) 32% porosity. The loading of the LMR-NCM cathodes is ≈12 ± 1 mg cm^{-2} and that of the NCA cathodes 13.5 ± 0.5 mg cm^{-2}. The porosities are determined from the electrode thicknesses measured by a tactile dial gauge using Eq. 1.

CAMs without internal porosity (as is usually the case for NCAs[58,59]) would appear less densely packed than the secondary particles of CAMs with significant porosity within the secondary particles, as is hypothesized to be the case for the here examined LMR-NCM material. This argument assumes that there is no significant particle cracking, which indeed has not been observed even when calendering the electrodes to 32% porosity (see Figs. 5c and 5f).

Mercury porosimetry.—To quantitatively investigate the qualitatively observed phenomenon of different pore volume fractions in the SEM images (Fig. 5), three mercury intrusion measurements were carried out for the different uncalendered and calendered porosities (Fig. 6) to determine the respective pore size distributions within the cathode coatings. To compare the porosity measured by mercury porosimetry with the overall porosity determined by coating thickness measurements (via Eq. 1), the electrode sample mass normalized pore volume (V_{pore}/m_{sample}, where m_{sample} is the mass of the two electrode coatings and the current collector foil) obtained by mercury porosimetry has to be corrected by the mass fraction of the aluminum current collector in the electrode (13.8 $wt\%_{alu}$ for the LMR-NCM and 12.6 $wt\%_{alu}$ for the NCA coatings) according to Eq. 4, yielding the pore volume per mass of coating ($V_{pore}/m_{coating}$).

$$\frac{V_{pore}}{m_{coating}} = \frac{V_{pore}}{m_{sample}} * \frac{1}{wt\%_{alu}} \qquad [4]$$

Equation 5 can then be used to calculate the cathode porosity, using the average bulk density of the coating ($V_{coating}/m_{coating}$):

$$\varepsilon_{coating(Hg)} = \frac{V_{pore}/m_{coating}}{V_{coating}/m_{coating}} = \frac{V_{pore}/m_{coating}}{\frac{1}{\rho_{bulk,sample}} - \frac{wt\%_{alu}}{\rho_{alu}}} \qquad [5]$$

where $\rho_{bulk,sample}$ is the measured mass of the electrode sheet samples in the measurement bulb divided by the sample volume, determined from the bulb volume minus the measured mercury volume at a low pressure of 0.029 MPa (where pores < 50 μm pore diameter are not filled with mercury).

In the literature, the coating porosities deduced from mercury porosimetry data are either calculated via the measured packing density of the coating (Eq. 5), as described by FROBOESE et al.,[62] or by adding the measured pore volumes to the calculated solid volumes using materials bulk densities, as done by SIMON et al.[63] The analysis in this paper is based on Eq. 5, as it has a wider application range (otherwise the exact electrode composition and the precise materials bulk densities must be known). However, the porosities calculated according to SIMON et al.,[63] are within 2 percentage points of the values calculated with Eq. 5. The small variation is a result of the different treatment of Hg-inaccessible pores by the two methods. While this porosity is simply neglected by the method of SIMON et al.,[63] Eq. 5 normalizes the measured porosity by a bulk density where the inaccessible pores are also neglected. For both calculation methods, a uniform mass loading needs to be assumed and therefore accuracy in porosity calculation is expected to be not higher than ±2 percentage points anyways (estimated by the variation of porosities calculated by Eq. 1 when measuring the coating thickness with the tactile dial gauge).

Figure 6 shows the logarithmic differential pore volume intrusion (d*Vol*/dlog*R*) vs the pore diameter that is plotted on a logarithmic scale, so that the areas under the curves in Fig. 6 are proportional to the intruded volume. Based on the analysis outlined below, it is proposed that the pore size distributions in Fig. 6 can be partitioned into three characteristic pore size regions for further evaluation: i) a region with small pores (<240 nm pore diameter), shown by the yellow shaded areas; ii) a region with intermediate pore sizes (light gray areas) with pores between 240 nm up to 8 μm for LMR-NCM coatings and up to 16 μm for NCA coatings; and, iii) a region extending from the intermediate pore size region all the way up to

50 μm (dark gray areas), which includes effects from the coating surface roughness and is thus referred to as "extra porosity" from thereon.

A porous sample composed of (secondary) aggregates of particles frequently shows a pore size distribution with multiple characteristic peaks,[64] whereby such multimodal pore size distributions vary depending on the material.[65] It should be noted that the characteristic pore radius that is obtained by mercury porosimetry represents the opening width distribution of the pores. Therefore, mercury porosimetry always measures the largest entry diameter into a given pore and not the actual pore size.[65] In general, mercury porosimetry can be used to investigate the pore opening width of porous materials between ≈500 μm and 3 nm as well as the pore volume distribution.[63]

In the case of the here conducted measurements on electrodes, for which ≈1–1.5 g electrode pieces (cut to ≈2–2.5 cm^2) had to be placed into the measurement bulb in order to obtain a sufficient accuracy, there is the additional complication of creating "pore volume" between the various electrode pieces, which needs to be distinguished from the pore volume of the electrode coatings. In a first step to avoid a significant contribution of pore volume arising from filling the gap between the electrode sheets in the measurement bulb, pores above 50 μm will be neglected, as they are in the range of the thickness of the electrode coating and thus cannot represent pores within the electrode coating. To further reduce this upper cut-off diameter is unfortunately not possible, since both of the investigated uncalendered cathodes have a defined pore volume distribution in this area. We believe that these rather large pore sizes are mainly an effect of the surface roughness of the electrodes, as it vanishes for the LMR-NCM coatings calendered to ≈42% and ≈32% as well as for the NCA coatings calendered to ≈32%. It should be noted that these surface roughness effects will also affect the porosities calculated by Eq. 1, where the measured thickness of the coating is used. Unfortunately, there is no common understanding in the literature on how to deal with the challenge of potentially overlapping pore regions. SIMON et al.[62] did not consider pore sizes beyond 10 μm when analyzing their mercury porosimetry data, but also had no defined peaks at larger pore diameters. FROBOESE et al.[61] claim that pore diameters exceeding the d$_{90}$ diameter (d$_{90, LMR-NCM}$ = 15 μm, d$_{90, NCA}$ = 23 μm) of the electrode materials are associated with the volume between the electrode pieces in the measurement bulb. This would exclude the above described pore volumes between 23–50 μm pores. However, since for practical electrode applications, electrodes are calendered quite strongly, the different data treatment approaches in the large pore size region would not yield very different results, as there is no porosity above 20 μm for strongly calendered electrodes, i.e., for electrodes with substantially lower final porosities compared to their as-coated porosity (in this case, this applies to the LMR-NCM electrodes with ≈42% and ≈32% porosity and to the NCA electrodes with ≈32% porosity).

The remaining contribution of the gap volume between the measured electrode sheets to the electrode coating pore volume below 50 μm is estimated by measuring uncoated aluminum current collector sheets with the same setup (Fig. A·2 in the Appendix). The contribution of the gap between the aluminum sheets that is proportional to the sample mass for a given electrode loading depends on the overall coating properties and contributes ≈2–6 percentage points to the overall porosity (≈6% for calendered samples with the lowest porosities and ≈2% for uncalendered electrodes with high porosity), a value which is subtracted from the pore volume in the pore size range between 8-50 μm (for more details see the explanation for Fig. A·2 in the Appendix). The total pore volumes (porosities) and their fraction for each pore size area (Table III) are corrected by these inter aluminum sheet pore contributions.

Next we will discuss the pore sizes and the pore volumes that we ascribe to the pores between the secondary agglomerates of the cathode active materials in the electrode, marked by the light gray
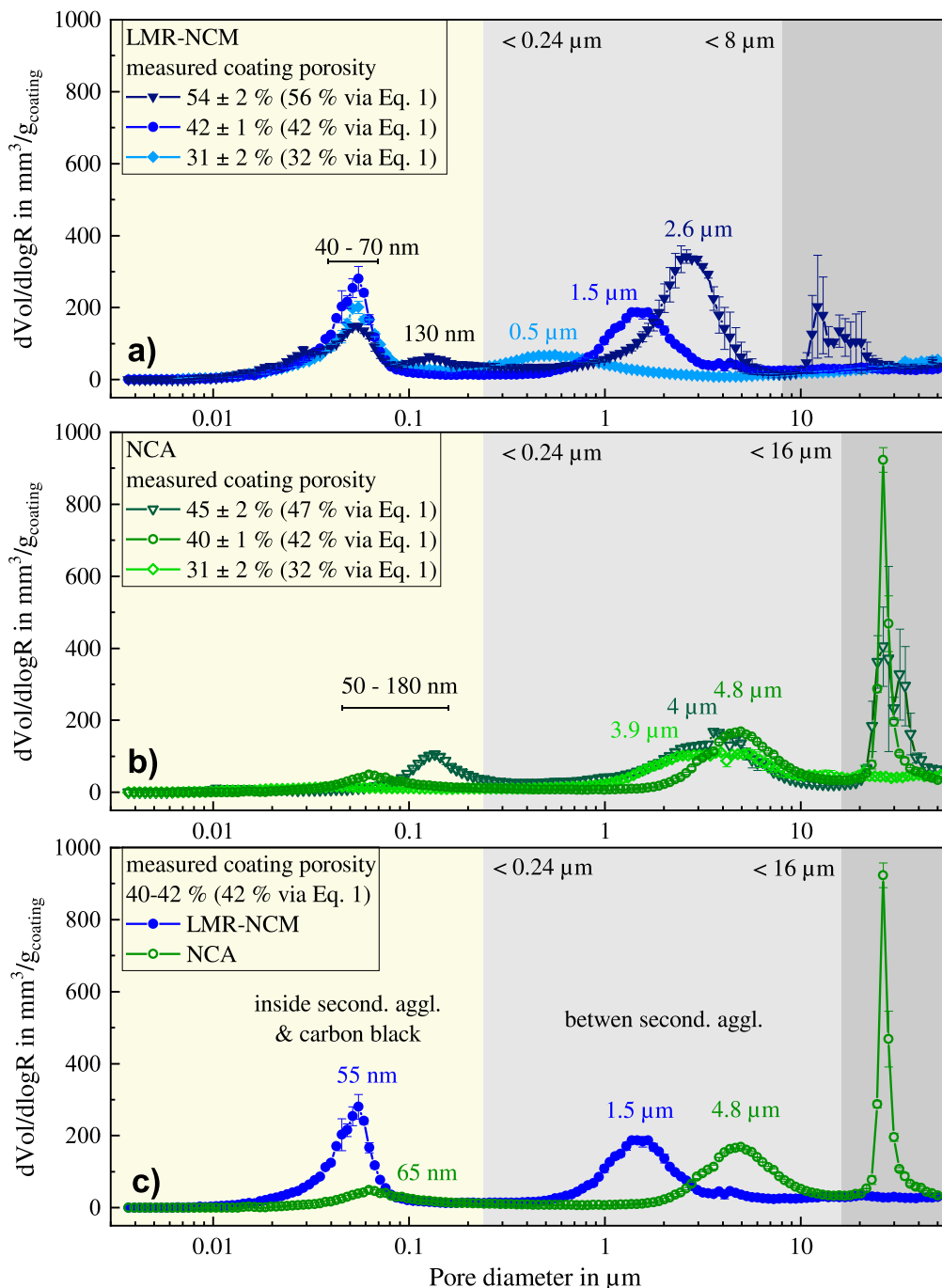
Figure 6. Mercury porosimetry based pore size distributions of uncalendered and calendered LRM-NCM and NCA electrode sheets, based on three independent repeat measurements for each electrode type (the standard deviations are marked by error bars): (a) for LMR-NCM coatings; (b) for NCA coatings; (c) comparing the pore size distribution for LMR-NCM and NCA cathodes with an overall porosity of 40%–42%.

areas in Fig. 6. For the LMR-NCM coatings (Fig. 6a), this region ranges between $\approx 0.24\ \mu m$ and $8\ \mu m$, while it extends up to $\approx 16\ \mu m$ for the NCA coatings (Fig. 6b). The assumption that the pores in the light gray region represent the pore volume between the secondary CAM agglomerates is supported by a simple estimation of the pore diameter of a close packing of spherical particles with tetrahedral voids ($d_{void} = 0.255 \cdot d_{particle}$) and octahedral voids ($d_{void} = 0.414 \cdot d_{particle}$): this predicts pore diameters of ≈ 2.5–$4\ \mu m$ for the LMR-NCM particles based on their d_{50} value of $\approx 10\ \mu m$, which is in reasonable agreement with the pore size maxima ranging between 0.5–2.6 μm shown in Fig. 6a; furthermore, larger pore diameters of ≈ 4–$6.5\ \mu m$ are predicted for NCA particles based on their d_{50} value of $\approx 15\ \mu m$, which again is in reasonable agreement with the

3.9–4.8 μm pore size maxima shown in Fig. 6b. The pore volume as well as the average pore diameter is shifted to smaller values by compression and hence represents the reduction of the space between the secondary agglomerates.

Last we will consider the volume in pores below $\approx 240\ nm$ (yellow region in Fig. 6), which so far were mostly considered as a contribution of the conductive carbon black matrix.[66] To differentiate the pore contributions of the electrode components, an NCA electrode without carbon black and a pure carbon black coating were measured, both uncalendered and calendered (Fig. A·3). Based on these measurements, it can be stated that the small peak at $\approx 130\ nm$ of the uncalendered LMR-NCM electrodes (dark blue triangles in Fig. 6a) arises from carbon black contributions. Therefore, the peak

Table III. Mercury porosimetry derived pore volumes (V_{pore}, in mm^3/g$_{coating}$) and porosities ($\varepsilon_{coating\,(Hg)}$ via Eq. 5) of LMR-NCM (abbreviated as LMR) and NCA electrodes divided into three regions, marking: i) the inner porosity of the secondary CAM agglomerates and contributions by the carbon black (yellow area in Fig. 6); ii) the porosity between the secondary CAM agglomerates (light gray area in Fig. 6); and, iii) the 'extra pores due to surface roughness of the coating (dark gray area in Fig. 6). The summed-up porosities/volumes measured by mercury porosimetry in the last column can be compared with the porosities calculated from thickness measurements via Eq. 1 (1st column). The pore volume contribution obtained with uncoated aluminum (see Fig. A·2 in the Appendix) was subtracted.

Overall $\varepsilon_{coating}$ via Eq. 1	Hg V_{pore} & $\varepsilon_{coating\,(Hg)}$ via Eq. 5	Pores within second. aggl. & carbon black		Pores between second. aggl.		"Extra" pores between second. aggl.		$V_{pore,\ overall}$ & $\varepsilon_{coating\,(Hg)}$ via Hg porosimetry	
		3−240 nm		0.24–8/16 μm		8/16–50 μm		3 nm−50 μm	
LMR/NCA		LMR	NCA	LMR	NCA	LMR	NCA	LMR	NCA
56/47%	vol. in mm^3/g$_{coating}$	81	35	156	100	47	62	**284 ± 12**	**198 ± 9**
	$\varepsilon_{coating\,(Hg)}$	16%	8%	30%	23%	8%	14%	**54%**	**45%**
42%	vol. in mm^3/g$_{coating}$	82	23	100	86	16	55	**199 ± 3**	**164 ± 3**
	$\varepsilon_{coating\,(Hg)}$	17%	6%	21%	22%	4%	13%	**42%**	**40%**
32%	vol. in mm^3/g$_{coating}$	76	15	50	88	18	17	**143 ± 7**	**121 ± 6**
	$\varepsilon_{coating\,(Hg)}$	16%	4%	10%	24%	5%	4%	**31%**	**31%**

at ≈55 nm is considered as porosity within the secondary LMR-NCM agglomerates, consistent with the observation that upon calendering this peak does not shift to smaller pore diameters and, more importantly, that the pore volume associated with this peak does not change significantly upon calendering (decreasing only from 81 to 76 mm³/g$_{coating}$, as shown later on in Table III). On the other hand, for the NCA electrodes (Fig. 6b) there is no peak in this area that is independent of calendering. Instead, the uncalendered NCA electrode shows a peak at also ≈130 nm that upon calendering shifts towards smaller pore sizes with smaller associated pore volumes (decreasing from 35 to 15 mm³/g$_{coating}$, as shown later on in Table III). As this follows the behavior of the pure carbon black coating (see Fig. A·3) and as the NCA coating without carbon black (see Fig. A·3) also shows no defined porosity in this pore size region, the porosity of the carbon black containing NCA electrode in the yellow region of Fig. 6b (i.e. below ≈240 nm) can clearly and solely be assigned to the contribution from the carbon black.

A direct comparison of LMR-NCM and NCA electrodes calendered to a mercury porosimetry based porosity of 40–42% (Fig. 6c) illustrates the difference in the pore size distribution of the two materials. In the light gray region that marks the pores between the secondary CAM agglomerates, both CAMs appear to have very similar pore volumes (note that the area under the curves in this plot is proportional to the pore volume). On the other hand, in the yellow region that marks the pore volume due to the carbon black contribution for both electrodes in addition to the pore volume within the secondary CAM agglomerates, the pore volume of the LMR–NCM electrode is substantially larger than that of the NCA electrode, which as discussed above is due to its significant porosity within the secondary agglomerates (note that the same mass ratio of carbon black was used in both electrodes).

For a more quantitative comparison of the pore volumes in the different pore size regions of uncalendered and calendered LMR-NCM and NCA electrodes, Table III provides the Mercury porosimetry based pore volume (V_{pore}, in mm³/g$_{coating}$) and porosity ($\varepsilon_{coating\ (Hg)}$, via Eq. 5) contribution to each pore size region; these are summed up in the last column to the total mercury porosimetry based V_{pore} and $\varepsilon_{coating\ (Hg)}$. The overall coating porosity determined by Eq. 1 ($\varepsilon_{coating}$) that is given in the first column agrees within 1–2 percentage points with that determined by mercury porosimetry. On average, the porosity determined from mercury porosimetry (last column) is always slightly lower than that determined from tactile gauge measurements and bulk material densities (first column), which may be due to the fact that pores below 3 nm are not accessed in mercury porosimetry measurements and that occluded void volumes in the CAM materials result in a lower bulk material density compared to the crystalline density, which would lead to an overestimate of the porosity when determined by Eq. 1. Despite these minor differences, the overall porosities obtained by these two methods are in quite good quantitative agreement (i.e., within a relative difference of <5%).

Next we will examine the Mercury porosimetry based pore volumes (V_{pore}) and porosity contributions ($\varepsilon_{coating\ (Hg)}$) for uncalendered and calendered electrodes in the lowest pore size region (highlighted in yellow in Fig. 6), which we associate with the volume of the pores inside the secondary agglomerates and/or within the carbon black agglomerates. In case of the NCA electrodes, the relative contribution of V_{pore} in this region to the overall pore volume (i.e., $V_{pore}/V_{pore,\ overall}$) decreases from ≈18% for uncalendered electrodes to ≈14% and ≈12% for electrodes calendered to ≈42% and ≈32% porosity, respectively. As shown by the experiments with NCA electrodes without carbon black and with pure carbon black electrodes (see Fig. A·2 in the Appendix), the pore volume of NCA electrodes in this low pore size region can clearly be attributed to the pore volume contributions by the carbon black additive. Thus, for calendered NCA electrodes, the pore volume in the low pore size region and its contribution to the overall pore volume is rather small (namely <12% with respect to the overall porosity as decreasing electrode porosity above 32% can be

attributed to the CB porosity). On the other hand, for the LMR-NCM electrodes, V_{pore} in this region decreases very little upon calendering (from 81 to 76 mm³/g$_{coating}$), so that $V_{pore}/V_{pore,\ overall}$ in the low pore size region *increases* from ≈29% for uncalendered electrodes to ≈41% and ≈53% for electrodes calendered to ≈42% and ≈32% porosity, respectively. This large fraction of pores within the secondary LMR-NCM agglomerates explains why the calendering of LMR-NCM electrodes to ≈32% porosity leads to aluminum foil embossing (see Fig. 4b), as ≈53% of the pore volume at the overall porosity of ≈32% is contained within pores of the secondary LMR-NCM agglomerates that do not break under these calendering conditions (see Fig. 5c).

The intermediate pore size region (≈0.24–8/16 μm, pores between secondary agglomerates in Table III and marked by the light gray area in Fig. 6) is associated with the pores between the secondary CAM agglomerates. For the NCA electrodes, $V_{pore}/V_{pore,\ overall}$ in this region is ≈51%–52% for uncalendered (≈47% porosity) and for lightly calendered electrodes (≈42% porosity), and then increases to ≈73% upon strong calendering to ≈32% porosity. This delayed response of $V_{pore}/V_{pore,\ overall}$ upon calendering is attributed to the fact that the first calendering step only reduces the NCA porosity by very little, contrary to the second calendering step, where the porosity is decreased substantially. On the other hand, for LMR-NCM electrodes, $V_{pore}/V_{pore,\ overall}$ in the intermediate pore size region decreases from ≈55% for the uncalendered electrodes to ≈50% and ≈35% for the electrodes calendered to ≈42% and ≈32% overall porosity, respectively. This is accompanied by a strong shift of the average pore size from ≈2.6 μm to ≈0.5 μm (see Fig. 6a).

Summarizing the above findings for the strongly calendered electrodes (≈32% porosity), the majority of the pore volume for the NCA electrodes is in the intermediate pore size region (≈73%), while it is in the low pore size region for the LMR-NCM electrodes (≈35%). At the same time, $V_{pore}/V_{pore,\ overall}$ in the large size pores ("extra" pores between secondary agglomerates in Table III and dark gray area in Fig. 6) for both LMR-NCM and NCA electrodes calendered to ≈32% porosity has decreased to only ≈13%–14%.

Formation and degassing of multilayer pouch cells.—The challenges of the extensive gas release during the first-cycle activation of LMR-NCM cathodes have already been extensively discussed from a mechanistic point of view in the literature.[10,23,67–69] In this work, we instead address this aspect from an engineering point of view, as the amount of gas released from LMR-NCM cathodes in large-format cells can be quite substantial and can pose a serious problem during their formation. This is perhaps less critical for hardcase cells that undergo formation in an open state (under protective atmosphere) and are only sealed after the complete formation procedure, in addition to having over-pressure safety devices.[70] For pouch cells, however, the formation process is executed in a temporarily sealed state without external pressure on the pouch cell and with a gas pocket provided as space for the gas generated during formation; after formation, the gas generated during formation is eliminated by removing the gas pocket and then tightly re-sealing the pouch cells under vacuum (≈80 mbar).[49] As NCM or NCA based cells operate at maximum delithiation degrees of < 80%, the cathode active materials show little gassing,[71] so that most of the gas released in the formation cycle is due to SEI formation on the anode.[72] However, LMR-NCM requires a first-cycle activation to 4.7 V and a subsequent upper cut-off voltage of 4.6 V, which particularly in the first cycle leads to oxygen release from the CAM lattice and concomitant electrolyte oxidation that is accompanied by substantial gas evolution.[17,66] This oxygen release was also shown to require EC free electrolytes for cells with LMR-NCM cathodes in order to avoid rapid electrolyte degradation,[23] so that FEC based electrolytes are commonly used, despite the poorer thermal stability of FEC at operating temperatures above 45 °C.[73–75]

To better understand the amount of gas released during the initial cycles of LMR-NCM/graphite cells, OEMS measurements were

conducted to quantify the amount of released gas (CO_2, CO, H_2, and O_2) during the first-cycle formation (Fig. 7a) and the following three cycles (Fig. 7b) of LMR-NCM/graphite cells. The amount of released gas (in units of $\mu mol/g_{CAM}$) is given in Fig. 7c for the first activation cycle (left-most bars) conducted either at 25 °C (orange) or 45 °C (red), for the subsequent 3 cycles (cycles 2–4; middle bars) conducted at 25 °C following activation at 25 °C (orange) or 45 °C (red), and summed up for all 4 cycles (right-most bars). The lower dotted area in the left-most bars marks the total gas formation during the very initial charging of the cells to 4 V, which closely represent the gases released by anode SEI formation, as LMR-NCM cathode active materials do not show any gassing below ≈ 4.2 V vs Li^+/Li, i.e., below ≈ 4.1 V vs graphite.[10,17] Thus, the gas evolution due to SEI formation is ≈ 90 $\mu mol/g_{CAM}$ at 25 °C and slightly more at 45 °C (≈ 105 $\mu mol/g_{CAM}$); based on this, the expected evolved gas volume (referenced to 25 °C and 1 bar) in our multilayer pouch cells with 27.6 g LMR-NCM would amount to ≈ 62 ml and ≈ 72 ml, respectively (shown on the right-hand axis of Fig. 7c).

The gas evolved during the first-charge in the segment between 4 V during charge and 4 V during discharge is marked by the striped segments of the left-most bars in Fig. 7c. This is mostly due to gas evolved from the LMR-NCM cathodes (including cross-talk reactions with the anode), as the gas evolution due to anode SEI formation becomes very small once the graphite potential is below ≈ 0.2 V Li^+/Li[76] (as is the case once the cell potential is >4 V for the LMR-NCM cells). This amounts to ≈ 110 $\mu mol/g_{CAM}$ for the

activation at 25 °C, corresponding to a projected volume of ≈ 75 ml for our large-format pouch cells; the former is reasonably close to the ≈ 150 $\mu mol/g_{CAM}$ that TEUFL et al.[10] obtained within the same voltage limits for a similar LMR-NCM material and an FEC/DEC electrolyte without co-solvents and additives. When conducting the activation at 45 °C, ≈ 150 $\mu mol/g_{CAM}$ are evolved (striped segment in the left-most red bar), corresponding to a projected volume of ≈ 103 ml for our large-format pouch cells. Finally, in the last segment of the first activation cycle, namely between 4 V and 2 V during discharge, a rather small additional amount of gas is evolved from the LMR-NCM cathodes, as is indicated by the top segment of the left-most bars in Fig. 7c (this is consistent with the study by TEUFL et al.[10]).

Based on this analysis, the larger fraction of the gas evolved during the first-cycle activation of LMR-NCM/graphite cells is caused by the extensive gassing of LMR-NCM cathodes. Furthermore, the major amount of cathode derived gas is formed between 4 V during charge and 4 V during discharge and could be removed with a second degassing step at 4 V during the discharge process. The unmarked area in the formation cycle in Fig. 7c (after 4 V while discharging) is most likely delayed cathode gassing. The cell formation procedure adopted here for large-format LMR-NCM/graphite cells aimed to shift the gassing after the first formation cycle (i.e., from cycles 2–4 in Fig. 7c) into the formation cycle, so that the gas can be vented prior to the final sealing of the cells. This can be accomplished by conducting the first formation cycle at 45 °C rather than at 25 °C, leading to a $\approx 52\%$ reduction of the gas that is
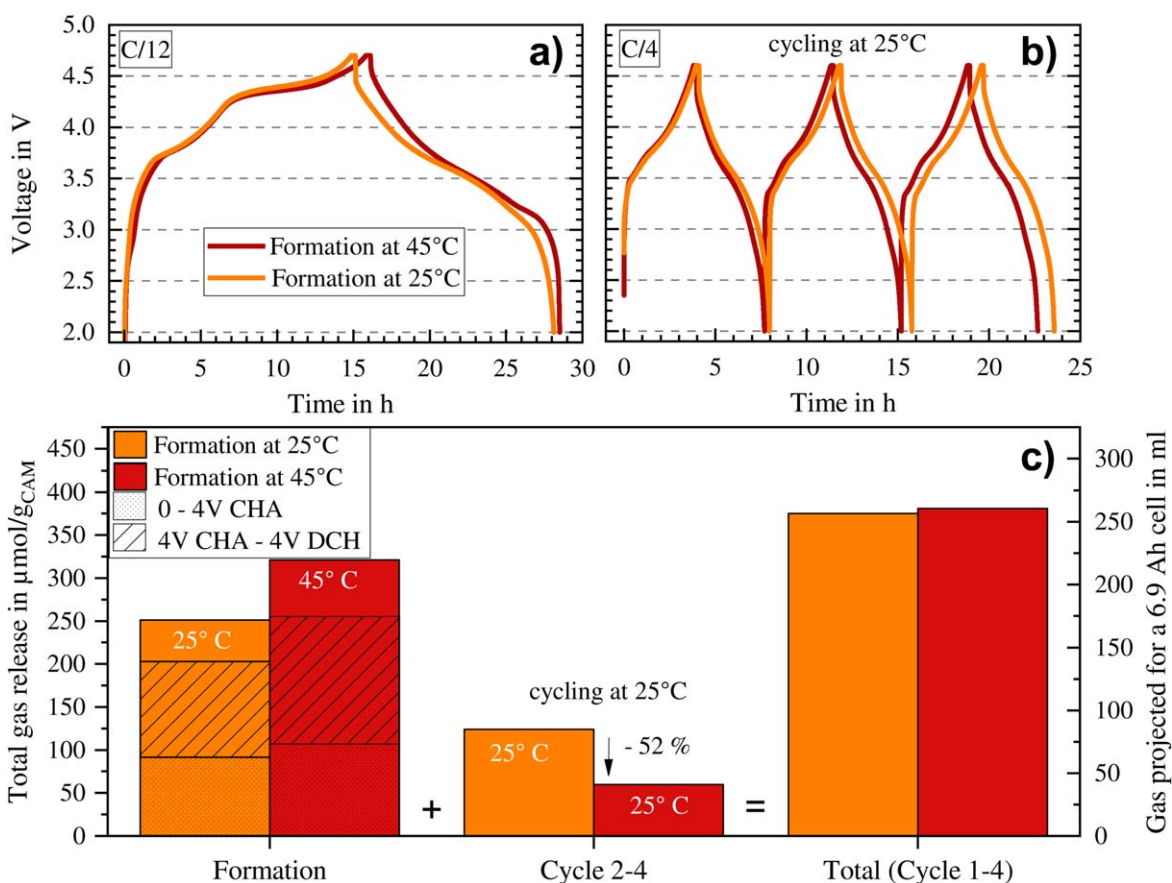

Figure 7. OEMS measurements with LMR-NCM working electrodes and graphite counter electrodes using the FEC/DEC based LMR-NCM electrolyte that was used for the coin and multilayer pouch cells. (a) Cell voltage profile vs time during a formation cycle at 25 °C (orange) or 45 °C (red) with a C-rate of C/12 and a CV step at 4.7 V till C/24. (b) Cell voltage profile vs time for three cycles at 25 °C with C/4 and a CV step at 4.6 V till C/8, following the first-cycle activation at 25 °C (orange) or 45 °C (after a 4 h rest period at OCV). (c) Total amount of released gas (i.e., sum of CO_2, CO, H_2, and O_2 in units of $\mu mol/g_{CAM}$) over the first-cycle activation, over cycles 2–4, and summed up for all cycles 1–4. The lower dotted area in the bars for the first-cycle formation shows the gas release up to 4 V during the first charge, the striped areas represent the released gas in the first-cycle between 4 V during charge and 4 V during discharges, while the non-marked upper region of the bars indicates the gas released between 4 V and 2 V during the first-cycle discharge. The right axis corresponds to the gas volume (evaluated at 25 °C and 1 bar) that would be generated in the here produced multilayer pouch cells with 27.6 g LMR-NCM (corresponding to ≈ 6.9 Ah at 0.1C).
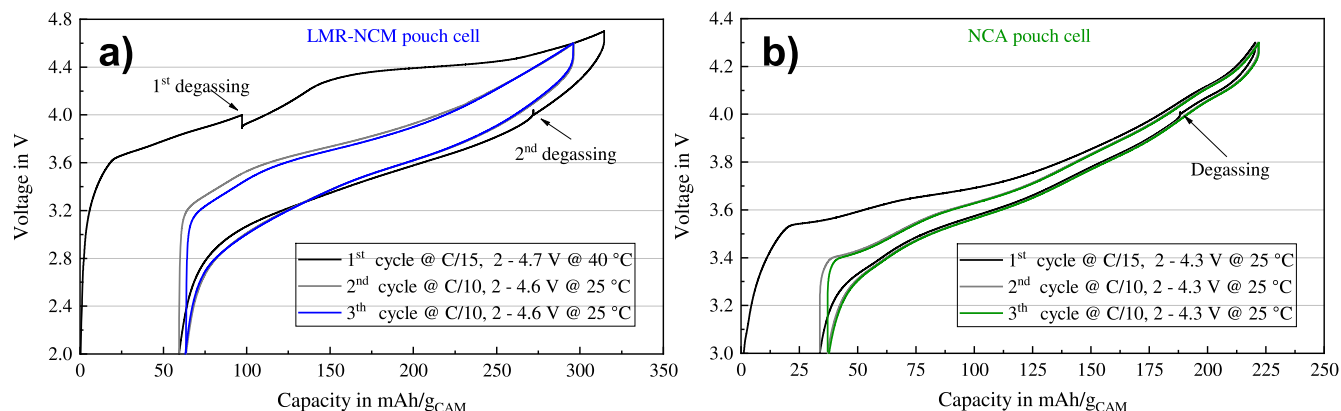
Figure 8. Formation cycle followed by two stabilization cycles of LMR-NCM (a) and NCA (b) pouch cells, indicating the degassing steps at 4.0 V in the formation cycle. The cells were cycled without external compression until the last degassing step and afterward compressed in a cell holder with 0.2 MPa.[52]

released in cycles 2–4 (see middle bars in Fig. 7c), namely from ≈85 ml to ≈41 ml projected for the here used large-format pouch cells. We found that our large-format LMR-NCM/graphite pouch cells (≈6.9 Ah at 0.1C) would burst open after several cycles due to excessive internal gas pressure when activated at 25 °C, while this did not occur until ≈250 cycles when activated at elevated temperature.

The formation strategy for LMR-NCM/graphite pouch cells developed for this work, therefore, dealt with the additional gassing from the cathode side by conducting a slow formation at 40 °C with two degassing steps, as shown in Fig. 8a. These two steps were incorporated to avoid the accumulation of the anode and the cathode derived gas over the course of the first cycle in order to: i) avoid a further reaction of the evolved gasses with the electrolyte and the electrode interfaces, and ii) to reduce the total amount of gas that might block parts of the anode from contact to the electrolyte, thereby reducing the area of the anode accessible for a homogeneous lithiation. A formation temperature of 40 °C (instead of the 45 °C used for the OEMS study) was selected for the multilayer LMR-NCM pouch cells to assure that, even in the presence of the expected temperature gradients across the thickness of the cell, the temperature would not exceed at any location the critical 45 °C for an FEC based electrolyte. Fig. 8a shows exemplarily the finally chosen formation and stabilization cycles for one of the LMR-NCM multilayer pouch cells. For comparison, the regular formation procedure applied for the NCA pouch cells, with only one degassing step in the first discharge at 4 V, is shown in Fig. 8b.

Particularly in the production of large-format pouch cells, a compromise must be found between a fast removal of the gas and cost-effective processing: since the cells have to be opened and closed for each degassing step, additional degassing steps require more cell packaging material. In each degassing step, the cell is pierced and sealed in the subsequent step, whereby the affected zone moves closer to the cell stack with each repetition. Furthermore, it has to be considered that cell opening and sealing at high SOC poses a significant safety risk, as the energy released in the event of a short circuit scales directly with SOC. Therefore, from a production safety perspective, degassing at low SOCs is desirable to perform the fully automated process, which is of course in contrast to the economic point of view that aims to close the formation process as soon as possible.

Specifications and initial performance of large-format multilayer pouch cells.—The LMR-NCM/graphite and the NCA/graphite large-format multilayer pouch cell specifications were determined on the basis of the coin half-cell data at 0.1C (shown in Table II, based on the 3rd cycle in Fig. 3). After formation of the pouch cells, their initial performance at 0.1C (exemplarily shown for one set of cells in Fig. 8) was then compared with the performance characteristics

projected in Table II in combination with the Excel-based *cell configuration tool* given in the supporting information. A summary of the targeted pouch cell specifications and the projected pouch cell performance vs that of the actually produced cells is shown in Table IV.

The actually achieved/measured values for the large-format multilayer pouch cells are based on the mean value of 16 LMR-NCM/graphite pouch cells and of 16 NCA/graphite pouch cells. Generally, the projected values for the LMR-NCM cells were accurate and match very well with the actually measured values. A smaller deviation, however, can be observed for the cell mass that is ≈2.3% lower than targeted, which we believe is due to electrolyte evaporation during filling and during the two degassing steps. For the NCA/graphite pouch cells, the CAM based capacity matches quite well with the projections, but the cell specific capacity shows a discrepancy of 2.7%. This deviation can simply be explained by a loading overbalancing on the anode electrode, whose actual loading was slightly too high (10.2 mg cm^{-2} instead of the desired 8.8 mg cm^{-2}), leading to an areal capacity overbalancing of anode to cathode of 1.4/1 instead of the desired 1.2/1. The unused anode leads to a negligible change in cell performance (max. 1.8% capacity loss due to additional SEI losses), but to a higher than projected cell mass, and thus to a lower than projected cell energy density.

The cell data based on the 3rd formation cycle of the LMR-NCM/graphite multilayer pouch cells show promising results, since a higher energy density was achieved with a potentially lower cost CAM (owing to a high manganese content). However, while the specific capacity of the LMR-NCM pouch cells is ≈30% higher in comparison to the NCA pouch cells, the lower mean discharge voltage of the LMR-NCM cells results in only ≈10% higher energy density on the cell level. The first-cycle coulombic efficiency (CE) of the LMR-NCM cells was 83.9 ± 1.9%, quite comparable with the CE of the NCA cells of 84.9 ± 0.3%. The larger standard deviation of the CE of the LMR-NCM cells can be explained by the fact that the cells experienced a cell temperature change during the first cycle (40 °C until the second degassing step, followed by 25 °C until the end of the first cycle).

In summary, scale-up projections on the basis of coin half-cell data have been shown to predict the initial performance of large-format cells quite accurately. This is of course only valid, as long as aging effects and cell setup dependent temperature effects can be neglected. Further cell characteristics, such as rate capability, long-term cycling, as well as thermal behavior are discussed in Part II of this work.[52]

Conclusions

To the best of our knowledge, this work examines for the first time the various challenges encountered during the production and formation of large-format multilayer pouch cells with a lithium- and

Table IV. Targeted specifications and 0.1C performance projections for large-format multilayer LMR-NCM/graphite and NCA/graphite pouch cells, based on the coin half-cell data (given in Table **II**, based on the 3rd cycle in Fig. **3**) and the *cell configuration tool* given in the supporting information. This is compared with the specifications of the actually produced pouch cells calendered to a porosity of ≈42% and their performance characteristics (averaged over 16 LMR-NCM and 16 NCA pouch cells, with the ± values marking the standard deviation of the averages).

Type	CAM mass[a] in g$_{CAM}$	Cell mass[b] in g$_{cel}$)	CAM spec. DCH capa.[c] in mAh/g$_{CAM}$	Cell spec. DCH capa.[c] in Ah	Mean disch. voltage[c] in V	Cell energy density[c] in Wh/kg$_{cell}$
LMR-NCM targeted/projected[d]	28	115	241	6.6	3.54	204
actual LMR-NCM pouch cell data	27.6 ± 0.5	112 ± 3	236 ± 4	6.5 ± 0.1	3.486 ± 0.009	202 ± 4
NCA targeted/projected[d]	31	113	188	5.8	3.73	190
actual NCA pouch cell data	30.8 ± 0.8	116 ± 1	188 ± 4	5.8 ± 0.2	3.695 ± 0.009	185 ± 6

a) determined by weighing the cathodes before stacking. b) determined by weighing the cells after formation. c) mean discharge value of the 2nd cycle at 0.1C after the first formation cycle. d) Calculated with the cell configuration tool in the supporting information, using the cell performance data according to Table **II** (3rd cycle of the cells with ≈42% porosity) and the loading and material specifications according to the pouch cell setup described in the experimental part.

manganese-rich NCM (LMR-NCM) cathode active material (CAM) and graphite anodes, using a pilot scale production line. The performance and energy density of these LMR-NCM/graphite cells with a nominal capacity of ≈6.9 Ah at 0.1C (based on a nominal specific capacity of 250 mAh/g_{CAM}) is compared to that of analogously produced large-format NCA/graphite cells with a similar nominal capacity of ≈6.1 Ah (based on a nominal specific capacity of 200 mAh/g_{CAM}). The pouch cell specifications were established using an Excel-based cell configuration tool in combination with initial performance data from LMR-NCM/lithium and NCA/lithium coin cells.

Coin half-cell tests investigating the rate capability of LRM-NCM cathodes as a function of CAM loading and degree of calendering (i.e., of cathode porosity) show, as expected, that the CAM specific performance is best for low loadings in combination with a high porosity. In contrast, with regards to the projected specific energy density for large-format cells (i.e., in Wh/kg_{cell}), the optimum values for C-rates up to 1C are obtained with LMR-NCM loadings of ≈12 mg cm^{-2} (corresponding to ≈3.0 mAh cm^{-2} at 0.1C) and with cathode coating porosities of ≈42%.

Calendering experiments with large-scale electrodes reveal a remarkably different behavior between LMR-NCM and NCA cathode coatings. While the latter can be calendered without difficulties to ≈32% coating porosity (as is the case for NCMs), LMR-NCM coatings cannot be calendered to this porosity without substantial aluminum foil embossing that prevents their use in large-format cells. This phenomenon is examined by a detailed analysis of the structure of the cathode coatings calendered to different porosities by means of SEM cross-sectional analysis and of mercury intrusion porosimetry based pore size distribution measurements. For electrodes calendered to ≈32% coating porosity, the latter reveals that the fractional pore volume contained in pores of less than ≈240 nm (representative of pores either within the secondary CAM agglomerates or contributed by the carbon black additive) is rather small for NCA coatings (≈11%), while it amounts to ≈50% for LMR-NCM coatings due to a large pore volume within the secondary LMR-NCM agglomerates. Therefore, without the undesired breakage of secondary agglomerates, porosities of ≈32% cannot be achieved for LMR-NCM coatings without extensive aluminum foil embossing effects.

Another critical aspect is the different formation requirement for large-format high-capacity pouch cells with NCA (or NCM) vs those with LMR-NCM cathode active materials. This is due to the extensive gassing of LMR-NCMs in the first few cycles, which necessitates a modification of the formation procedure in order to shift most of the CAM related gassing into the first cycle, i.e., before the final sealing of the cells. By means of on-line electrochemical mass spectrometry (OEMS) it was found that a first-cycle formation at elevated temperature is able to shift more than 50% of the CAM related gassing in the three cycles after the formation cycle into the formation cycle. This, combined with two degassing steps in the formation cycle for the LMR-NCM cells (instead of one for NCA) is shown to strongly reduce internal cell pressure build-up after the final sealing of the cells and thus enable long-term cycling stability.

To conclude, 16 LMR-NCM and NCA large-format pouch cells with a measured capacity at C/10 of 6.5 ± 0.1 Ah for LMR-NCM and 5.8 ± 0.2 Ah for NCA were produced at the pilot scale production line at the Technical University of Munich. The average CAM specific capacity at C/10 after formation is 236 ± 4 mAh/g_{CAM} for the LMR-NCM and 188 ± 4mAh/g_{CAM} for the NCA cells, close to their nominal specific capacities of 250 mAh/g_{CAM} and 200 mAh/g_{CAM}, respectively. This results in a ≈30% higher capacity of the LMR-NCM/graphite pouch cells. However, due to their lower average discharge voltage, the cell level energy density of 203 ± 4 Wh/kg_{cell} for LMR-NCM/graphite large-format cells is only ≈10% larger than that for the NCA/graphite cells (185 ± 6 Wh/kg_{cell}). While this difference is rather small, the lower CAM material costs

for the manganese-rich LMR-NCM compared to nickel-rich NCA is a significant advantage of LMR-NCM based CAMs.

The rate capability, long-term cycling stability, and thermal behavior of the LMR-NCM/graphite and NCA/graphite large-format cells produced here is presented in Part II of this study.[51]

Appendix

Mixing.—The mixing parameters solid content and mixing speed are plotted in Fig. A·1 vs the mixing time for the three materials used: LMR-NCM, NCA and graphite. One challenge in upscaling, for example, is the heat generated during the mixing process.

For highly viscous media, the heat generated during the mixing process has to be dissipated in order to avoid excessive heating of the slurry. Assuming a constant heat generation per volume, for larger batches the heat transfer via the vessel wall per volume is smaller due to the comparatively smaller surface of the slurry.[77] To avoid a temperature increase of the slurry with larger batch quantities, either the supplied mixing power must be reduced or the relatively smaller surface area must be compensated by a higher cooling rate. The latter approach is limited by the performance of the cooling system, while the first approach requires a reduced mixing intensity, leading to a longer mixing time. Both, elevated temperature and longer mixing times favor the occurrence of slurry gelation. This is particularly critical for nickel-rich cathode materials,[78] as they contain significant amounts of LiOH and Li_2CO_3 surface impurities, at part formed in their synthesis[79] and at part from brief exposure to ambient air,[80–82] which promote slurry gelation.[82] As cooling of the here used Speedmixer is not possible during the process, the cooling was carried out externally in a cooled water tank.

Mercury porosimetry.—To estimate the error due to the spacing between the electrode sheets that yields an apparent porosity at high pore diameter, the pore size distribution of uncoated aluminum sheets (the same number as that was used in the measurements with actual electrodes) was measured and is scaled in terms of mm^3/$g_{coating}$ by taking into the weight fraction of aluminum in the electrodes (black dots in Fig. A·2). In comparison with an uncalendered NCA coating (green triangles in Fig. A·2), the pore volume contribution from the aluminum sheets is only significant at high pore diameters, i.e. above ≈10 μm (black dots). Although the here used aluminum foil has of course no real porosity, the porosimetry measurements show a porosity of 28 ± 1% that corresponds to 9% porosity after adjusting the weight normalization
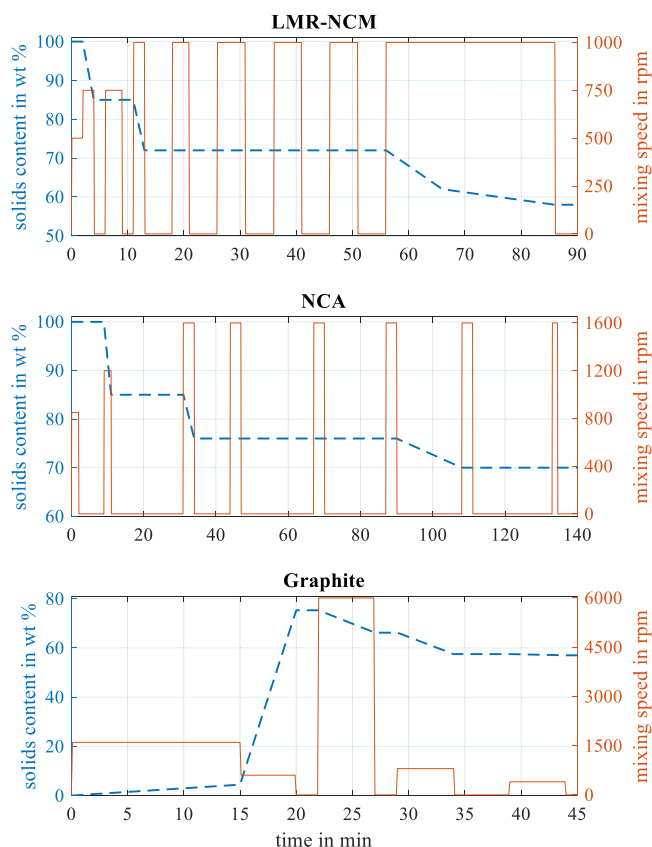
Figure A·1. Mixing process sequence for the LMR-NCM, NCA, and graphite slurries. The blue dotted line shows the solids content of the slurry over the mixing time. The orange line shows the mixing speed over the mixing time.

pore diameters in the range of the coating thickness are not considered to contribute to the actual porosity of the coating. The remaining contribution of aluminum up to 50 μm to the coating porosity is 50 mm^3/g$_{alu}$ and contributes $\approx$2–6 percentage points in porosity (6% for samples with low porosities, e.g. the NCA coating at 32% porosity, and 2% for uncalendered electrode coatings with high porosity). This contribution (50 mm^3/g$_{alu}$) is subtracted from the porosity in the "extra" pores between secondary agglomerates in Table III by multiplying it with the measured sample mass and the weight fraction of aluminum (13.8% in case of LMR-NCM and 12.6% in case of NCA).

To estimate the contribution of carbon black to the overall coating porosity, the pore size distribution of an NCA coating without carbon black and a pure carbon black coating are shown in Fig. A·3 both uncalendered and calendered. The pore size maximum of the non-calendered carbon black coating appears at a pore diameter of $\approx$180 nm and shifts to $\approx$60 nm and a lower overall pore volume upon calendering. There is no defined peak at $>$10 μm, which confirms our previous assumption that in the case of the NCA and LMR-NCM coatings the peak in this region is due to surface roughness of the coating that would be expected to be on the order of the secondary agglomerate size ($\approx$10–15 μm for the CAMs and on the order of 0.5–1 μm for the carbon black). On the other hand, an NCA coating without carbon black shows almost no porosity in the yellow area, therefore the porosity in Fig. 6b below 240 nm is mainly due to the carbon black in the electrode and not due to pores within the secondary agglomerates of the NCA material. This observation is in good agreement with nitrogen physisorption analysis, where the pores up to 150 nm could be quantified: for the pure NCA active material powder, a total pore volume in $\leqslant$ 150 nm pores of 1.13 $\pm$ 8 mm^3/g$_{CAM}$ was determined, whereas the same measurement on scratched-off NCA electrode material (scratched off with a scalpel from a regular, i.e. carbon black containing NCA coating) is $\approx$20-fold larger ($\approx$20–25 mm^3/g$_{coating}$). At the same time, the pore size maxima for the NCA electrode without carbon black (light gray area Fig. A·3) show the same behavior as the regular carbon black containing NCA electrode (see Fig. 6b) and can be attributed to pores in the coating between the secondary agglomerates of the cathode active material. The black arrows indicate the tendency of the pores between the secondary agglomerates to shift to smaller pore diameters and pore volumes
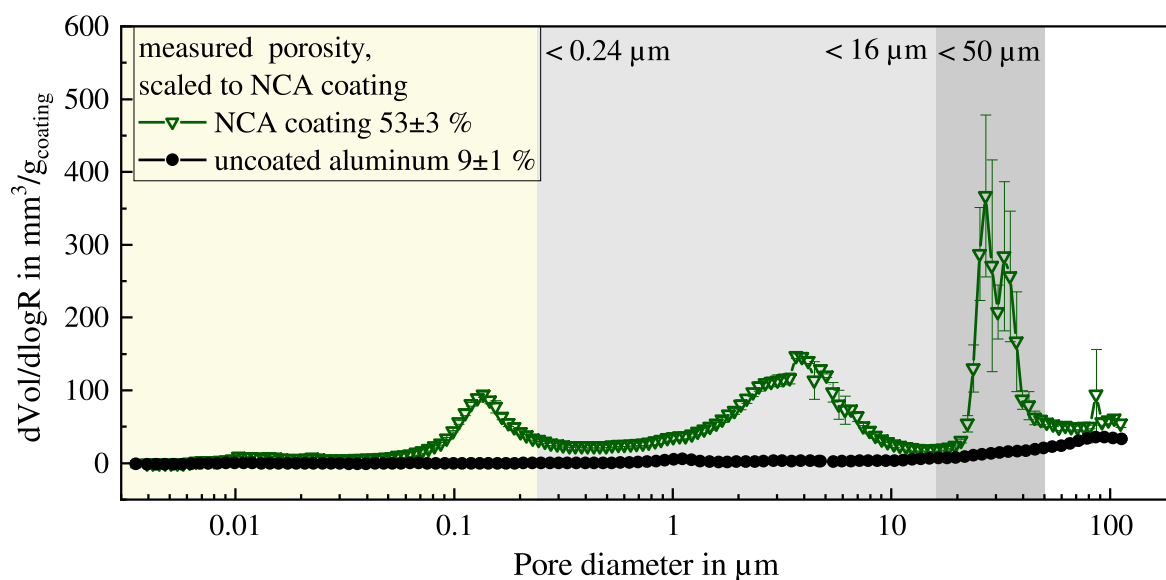
to the NCA coating (because 25 pieces without coating is for a pore range up to 112 μm. To avoid the significant contribution of the aluminum foil, the data in Fig. 6 are only analyzed up to a pore size of 50 μm, as we cannot see any defined pore areas above and also

Figure A·2. Mercury porosimetry of uncoated aluminum sheets in comparison with the uncalendered NCA electrode sheet that is also shown in Fig. 6b. The deviation of the introduced volume for the indicated pore size is plotted. The uncoated aluminum weight is normalized by the weight fraction of the aluminum sheets (12.6 wt%) in the NCA electrodes. The yellow shaded area marks the porosity within the secondary agglomerates and carbon black pores, the light gray shows the porosity between the secondary NCA agglomerates, and the dark gray area refers to extra pores between the secondary agglomerates.

Figure A·3. Mercury porosimetry of NCA electrodes without carbon black (NCA/PVdF of 92.5/3.5 wt%) and pure carbon black electrodes (CB/PVdF 66.7/ 33.2 wt%) both uncalendered and after calendering. The data were recorded between 3 nm and 100 μm pores, but only porosities up to 50 μm are considered to avoid artifacts of pores between the measured sheets. The yellow shaded area marks the porosity within the secondary agglomerates and carbon black pores, the light gray shows the porosity between the secondary NCA agglomerates, and the dark gray p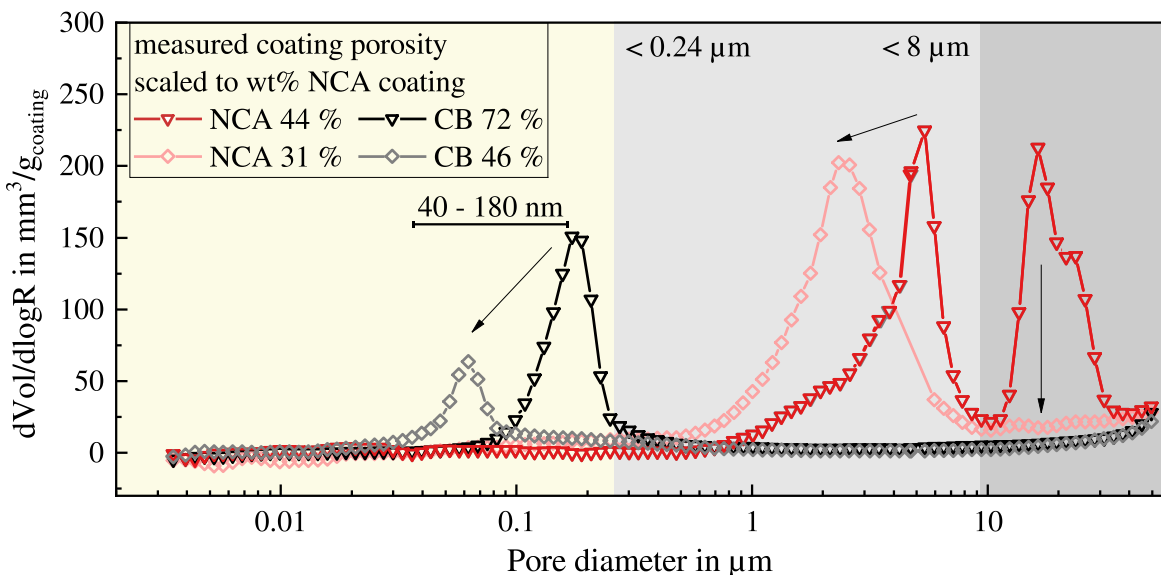art refers to extra pores between the secondary agglomerates and/or in between the electrode sheet samples. The impact of calendering for each coating type is marked by the black arrows. The porosity values given in the figure consider a pore diameter range from 3 nm–50 μm and the apparent porosity due to the void space between the electrode sample sheets is corrected for as described in the context of Fig. A·2.

upon calendering, which is also accompanied by a loss of porosity at >10 μm.

ORCID

David Schreiner https://orcid.org/0000-0001-8035-0438
Tanja Zünd https://orcid.org/0000-0002-1650-3636
Florian J. Günter https://orcid.org/0000-0002-5967-6801
Ludwig Kraft https://orcid.org/0000-0003-4324-426X
Benedikt Stumper https://orcid.org/0000-0002-4508-6210
Fabian Linsenmann https://orcid.org/0000-0001-8788-2584
Michael Schüßler https://orcid.org/0000-0002-4131-7392
Rebecca Wilhelm https://orcid.org/0000-0002-4161-5197
Andreas Jossen https://orcid.org/0000-0003-0964-1405
Hubert A. Gasteiger https://orcid.org/0000-0001-8199-8703

References

1. D. Andre, S.-J. Kim, P. Lamp, S. F. Lux, F. Maglia, O. Paschos, and B. Stiaszny, *J. Mater. Chem. A*, **3**, 6709 (2015).
2. R. Schmuch, R. Wagner, G. Hörpel, T. Placke, and M. Winter, *Nat. Energy*, **3**, 267 (2018).
3. K. G. Gallagher, S. Goebel, T. Greszler, M. Mathias, W. Oelerich, D. Eroglu, and V. Srinivasan, *Energy Environ. Sci.*, **7**, 1555 (2014).
4. S.-T. Myung, F. Maglia, K.-J. Park, C. S. Yoon, P. Lamp, S.-J. Kim, and Y.-K. Sun, *ACS Energy Lett.*, **2**, 196 (2017).
5. G.-L. Xu, X. Liu, A. Daali, R. Amine, Z. Chen, and K. Amine, *Adv. Funct. Mater.*, **30**, 2004748 (2020).
6. A. Kwade, W. Haselrieder, R. Leithoff, A. Modlinger, F. Dietrich, and K. Droeder, *Nat. Energy*, **3**, 290 (2018).
7. J.-H. Schünemann, *Phd. thesis*, Technische Universität Braunschweig (2015).
8. P. Rozier and J. M. Tarascon, *J. Electrochem. Soc.*, **162**, A2490 (2015).
9. F. Schipper et al., *Inorganics*, **5**, 32 (2017).
10. T. Teufl, B. Strehle, P. Müller, H. A. Gasteiger, and M. A. Mendez, *J. Electrochem. Soc.*, **165**, 2718 (2018).
11. Mangese price. accessed 02/09/2021SMM Information & Technology Co, Ltd., https://price.metal.com/Manganese.
12. Nickel price. accessed 02/09/2021SMM Information & Technology Co, Ltd., https://price.metal.com/Nickel.
13. X. Zhang, X. Meng, J. W. Elam, and I. Belharouak, *Solid State Ionics*, **268**, 231 (2014).
14. F. Dogan, B. R. Long, J. R. Croy, K. G. Gallagher, H. Iddir, J. T. Russell, M. Balasubramanian, and B. Key, *J. Am. Chem. Soc.*, **137**, 2328 (2015).
15. K. Kleiner, B. Strehle, A. R. Baker, S. J. Day, C. C. Tang, I. Buchberger, F.-F. Chesneau, H. A. Gasteiger, and M. Piana, *Chem. Mater.*, **30**, 3656 (2018).
16. M. Saubanère, E. McCalla, J.-M. Tarascon, and M.-L. Doublet, *Energy Environ. Sci.*, **9**, 984 (2016).
17. B. Strehle, K. Kleiner, R. Jung, F. Chesneau, M. Mendez, H. A. Gasteiger, and M. Piana, *J. Electrochem. Soc.*, **164**, A400 (2017).
18. L. Simonin, J.-F. Colin, V. Ranieri, E. Canévet, J.-F. Martin, C. Bourbon, C. Baehtz, P. Strobel, L. Daniel, and S. Patoux, *J. Mater. Chem.*, **22**, 11316 (2012).
19. P. Oh, S. Myeong, W. Cho, M.-J. Lee, M. Ko, H. Y. Jeong, and J. Cho, *Nano Lett.*, **14**, 5965 (2014).
20. D. Becker, M. Börner, A. Friesen, S. Klein, U. Rodehorst, M. Diehl, M. Winter, T. Placke, and R. Schmuch, *J. Electrochem. Soc.*, **167**, 60524 (2020).
21. J. Helbig, T. Beuse, V. Siozios, T. Placke, M. Winter, and R. Schmuch, *J. Electrochem. Soc.*, **167**, 60519 (2020).
22. L. Boulet-Roblin, M. E. Kazzi, P. Novák, and C. Villevieille, *J. Electrochem. Soc.*, **162**, A1297 (2015).
23. T. Teufl, D. Pritzl, P. Krieg, B. Strehle, M. A. Mendez, and H. A. Gasteiger, *J. Electrochem. Soc.*, **167**, 11 (2020).
24. F. T. Wagner, B. Lakshmanan, and M. F. Mathias, *J. Phys. Chem. Lett.*, **1**, 2204 (2010).
25. F. J. Günter, C. Burgstaller, F. Konwitschny, and G. Reinhart, *J. Electrochem. Soc.*, **166**, A1709 (2019).
26. S. Chen et al., *Joule*, **3**, 1094 (2019).
27. R. Petibon, V. L. Chevrier, C. P. Aiken, D. S. Hall, S. R. Hyatt, R. Shunmugasundaram, and J. R. Dahn, *J. Electrochem. Soc.*, **163**, A1146 (2016).
28. R. Jung, M. Metzger, D. Haering, S. Solchenbach, C. Marino, N. Tsiouvaras, C. Stinner, and H. A. Gasteiger, *J. Electrochem. Soc.*, **163**, A1705 (2016).
29. S. Solchenbach, D. Pritzl, E. J. Y. Kong, J. Landesfeind, and H. A. Gasteiger, *J. Electrochem. Soc.*, **163**, A2265 (2016).
30. B. J. Polzin, S. E. Trask, Y. Zhu, M. Bettge, D. P. Abraham, and A. N. Jansen, *Meet. Abstr.*, **MA2014-01**, 213 (2014).
31. K.-H. Pettinger, *Handbuch Lithium-Ionen-Batterien*, ed. R. Korthauer (Springer, Berlin) (2013).
32. O. Schmidt, M. Thomitzek, F. Röder, S. Thiede, C. Herrmann, and U. Krewer, *J. Electrochem. Soc.*, **167**, 60501 (2020).
33. G. Reinhart, T. Zeilinger, J. Kurfer, M. Westermeier, C. Thiemann, M. Glonegger, M. Wunderer, C. Tammer, M. Schweier, and M. Heinz, *Future Trends in Production Engineering*, ed. G. Schuh, R. Neugebauer, and E. Uhlmann (Springer, Berlin) pp. 3 (2013).
34. H. Zheng, L. Tan, G. Liu, X. Song, and V. S. Battaglia, *J. Power Sources*, **208**, 52 (2012).
35. D. Pritzl, A. E. Bumberger, M. Wetjen, J. Landesfeind, S. Solchenbach, and H. A. Gasteiger, *J. Electrochem. Soc.*, **166**, A582 (2019).
36. A. Jossen and W. Weydanz, *Moderne Akkumulatoren richtig einsetzen* (Cuvillier, Göttingen) (2019).
37. K. G. Gallagher et al., *J. Electrochem. Soc.*, **163**, A138 (2016).
38. Y. Wu, *Lithium-ion Batteries. Fundamentals and Applications* (CRC Press, Boca Raton, Florida) (2015).
39. S. Oswald, D. Pritzl, M. Wetjen, and H. A. Gasteiger, *J. Electrochem. Soc.*, **167**, 100511 (2020).

40. H. Bockholt, M. Indrikova, A. Netz, F. Golks, and A. Kwade, *J. Power Sources*, **325**, 140 (2016).
41. C. Meyer, H. Bockholt, W. Haselrieder, and A. Kwade, *J. Mater. Process. Technol.*, **249**, 172 (2017).
42. D. Schreiner, M. Oguntke, T. Günther, and G. Reinhart, *Energy Technol.*, **18**, 1900840 (2019).
43. T. Günther, D. Schreiner, A. Metkar, C. Meyer, A. Kwade, and G. Reinhart, *Energy Technol.*, **5**, 1900026 (2019).
44. C. Meyer, M. Weyhe, W. Haselrieder, and A. Kwade, *Energy Technol.*, **8**, 1900175 (2020).
45. W. Haselrieder, *PhD. thesis*, Technische Universität Braunschweig (2016).
46. T. Knoche and G. Reinhart, *Appl. Mech. Mater.*, **794**, 11 (2015).
47. F. J. Günter, S. Rössler, M. Schulz, W. Braunwarth, R. Gilles, and G. Reinhart, *Energy Technol.*, **8**, 1801108 (2020).
48. T. Knoche, F. Surek, and G. Reinhart, *Procedia CIRP*, **41**, 405 (2016).
49. R. Korthauer, *Lithium-Ion Batteries: Basics and Applications* (Springer, Berlin) (2018).
50. H. Koga, L. Croguennec, M. Ménétrier, P. Mannessiez, F. Weill, and C. Delmas, *J. Power Sources*, **236**, 250 (2013).
51. N. Tsiouvaras, S. Meini, I. Buchberger, and H. A. Gasteiger, *J. Electrochem. Soc.*, **160**, A471 (2013).
52. L. Kraft, T. Zünd, D. Schreiner, R. Wilhelm, F. J. Günter, G. Reinhart, H. A. Gasteiger, and A. Jossen, *Comparative Evaluation of LMR-NCM and NCA Cathode Active Materials in Multilayer Lithium-Ion Pouch Cells - Part II: Rate Capability, Long-Term Stability and Thermal Behavior.*, **168**, 020537.
53. J. Kaiser, V. Wenzel, H. Nirschl, B. Bitsch, N. Willenbacher, M. Baunach, M. Schmitt, S. Jaiser, P. Scharfer, and W. Schabel, *Chem. Ing. Tech.*, **86**, 695 (2014).
54. A. Guéguen, C. Bolli, M. A. Mendez, and E. J. Berg, "Elucidating the Reactivity of Tris(trimethylsilyl)phosphite and Tris(trimethylsilyl)phosphate Additives in Carbonate Electrolytes—A Comparative Online Electrochemical Mass Spectrometry Study." *ACS Applied Energy Materials*, **3**, 290 (2020).
55. D. Ye, G. Zeng, K. Nogita, K. Ozawa, M. Hankel, D. J. Searles, and L. Wang, *Adv. Funct. Mater.*, **25**, 7488 (2015).
56. A. Shah, M. N. Ates, S. Kotz, J. Seo, K. M. Abraham, S. Somu, and A. Busnaina, *J. Electrochem. Soc.*, **161**, A989 (2014).
57. E. Björklund, D. Brandell, M. Hahlin, K. Edström, and R. Younesi, *J. Electrochem. Soc.*, **164**, A3054 (2017).
58. J. B. Quinn, T. Waldmann, K. Richter, M. Kasper, and M. Wohlfahrt-Mehrens, *J. Electrochem. Soc.*, **165**, A3284 (2018).
59. M. M. Besli et al., *J. Mater. Chem. A*, **7**, 12593 (2019).
60. M. M. Besli et al., *Chem. Mater.*, **31**, 491 (2019).
61. J. Nanda, S. K. Martha, and R. Kalyanaraman, *Pramana - J Phys*, **84**, 1073 (2015).
62. L. Froboese, P. Titscher, B. Westphal, W. Haselrieder, and A. Kwade, *Mater. Charact.*, **133**, 102 (2017).
63. C. Simon, D. Kartouzian, D. Mueller, F. Wilhelm, and H. A. Gasteiger, *J. Electrochem. Soc.*, **164**, F1697 (2017).
64. H. Giesche, *Handbook of Porous Solids*, ed. F. Schüth, S. W. Kenneth, and J. Weitkamp (Wiley, Weinheim) p. 335 (2002).
65. H. Giesche, *Part. Part. Syst. Charact.*, **23**, 9 (2006).
66. H. Bockholt, W. Haselrieder, and A. Kwade, *ECS Trans.*, **50**, 25 (2013).
67. J. Wandt, A. T. S. Freiberg, A. Ogrodnik, and H. A. Gasteiger, *Mater. Today*, **21**, 825 (2018).
68. A. T. S. Freiberg, M. K. Roos, J. Wandt, R. de Vivie-Riedle, and H. A. Gasteiger, *J. Phys. Chem.*, **122**, 8828 (2018).
69. D. Streich, A. Guéguen, M. Mendez, F. Chesneau, P. Novák, and E. J. Berg, *J. Electrochem. Soc.*, **163**, A964 (2016).
70. J. Tuebke et al., *Entwicklungsperspektiven für Zellformate von Lithium-Ionen-Batterien in der Elektromobilität* (2017).
71. R. Jung, M. Metzger, F. Maglia, C. Stinner, and H. A. Gasteiger, *J. Phys. Chem. Lett.*, **8**, 4820 (2017).
72. R. Jung, M. Metzger, F. Maglia, C. Stinner, and H. A. Gasteiger, *J. Electrochem. Soc.*, **164**, A1361 (2017).
73. T. Teufl, D. Pritzl, S. Solchenbach, H. A. Gasteiger, and M. Mendez, *Meet. Abstr.*, **MA2018-02**, 456 (2018).
74. K. Kim, I. Park, S.-Y. Ha, Y. Kim, M.-H. Woo, M.-H. Jeong, W. C. Shin, M. Ue, S. Y. Hong, and N.-S. Choi, *Electrochim. Acta*, **225**, 358 (2017).
75. T. Teufl, D. Pritzl, S. Solchenbach, M. A. Mendez, and H. A. Gasteiger, *Thermal Stability of FEC-Based Electrolytes for High-Voltage Li-Ion Batteries.*, Manuscript in preparation.
76. M. Metzger, B. Strehle, S. Solchenbach, and H. A. Gasteiger, *J. Electrochem. Soc.*, **163**, A798 (2016).
77. R. Poggemann, A. Steiff, and P.-M. Weinspach, *Chem. Ing. Tech.*, **51**, 948 (1979).
78. J. Kim, H. Lee, H. Cha, M. Yoon, M. Park, and J. Cho, *Adv. Energy Mater.*, **8**, 1702028 (2017).
79. H.-J. Noh, S. Youn, C. S. Yoon, and Y.-K. Sun, *J. Power Sources*, **233**, 121 (2013).
80. J. Sicklinger, M. Metzger, H. Beyer, D. Pritzl, and H. A. Gasteiger, *J. Electrochem. Soc.*, **166**, A2322 (2019).
81. R. Jung, R. Morasch, P. Karayaylali, K. Phillips, F. Maglia, C. Stinner, Y. Shao-Horn, and H. A. Gasteiger, *J. Electrochem. Soc.*, **165**, A132 (2018).
82. Y. Chen, S. Song, X. Zhang, and Y. Liu, *J. Electrochem. Soc.*, **1347**, 012012 (2019).